Local and global spatio-temporal sensitivity analysis of thermal consolidation around a point heat source

3 authors:

Aqeel Afzal Chaudhry
Technische Universität Bergakademie Freiberg
9 PUBLICATIONS   **57** CITATIONS

SEE PROFILE

Jörg Buchwald
Helmholtz-Zentrum für Umweltforschung
27 PUBLICATIONS   **173** CITATIONS

SEE PROFILE

Thomas Nagel
Technische Universität Bergakademie Freiberg
171 PUBLICATIONS   **1,586** CITATIONS

SEE PROFILE

Some of the authors of this publication are also working on these related projects:

Project   MFrontGallery View project

Project   IGLU - Analysis, modelling and assessment if an intelligent and environmentally neutral geothermal long-term heat storage system View project

Local and global spatio-temporal sensitivity analysis of thermal consolidation around a point heat source

Aqeel Afzal Chaudhry[a,*], Jörg Buchwald[b,a], Thomas Nagel[a,c]

[a]*Chair of Soil Mechanics and Foundation Engineering, Geotechnical Institute, Technische Universität Bergakademie Freiberg, Germany*
[b]*Department of Environmental Informatics, Helmholtz Centre for Environmental Research GmbH – UFZ, Leipzig, Germany*
[c]*TUBAF-UFZ Center for Environmental Geosciences*

Abstract

Coupled thermo-hydro-mechanical (THM) models are used for the assessment of nuclear waste disposal, reservoir engineering, and many other branches of geotechnical engineering. Model-based decision making and optimization often entail sensitivity analyses (SA) and uncertainty quantification (UQ). The suitability of different UQ and SA methods for coupled THM problems on an engineering scale requires clarification. To provide such guidance without the need for large numerical studies, an analytical solution of a simple THM problem is employed here that encompasses the most relevant primary couplings, can robustly cover the entire parameter space, and remains computationally inexpensive. Both local (OVAT) and global sensitivity analysis (GSA) techniques are applied to the study of the THM model. The information that can be derived from the different approaches is then systematically assessed, such as parameters and interactions that control selected observation quantities and how their effect varies in both space and time. We provide application-oriented conclusions on the conditions which should be met when applying the different methods as well as examples for possible misinterpretations. The analysis can serve as a benchmark for UQ and SA software designed around numerical THM simulators. This work may also serve as an attempt to highlight the methodology and effectiveness of SA to the audience from an engineering background.

Keywords:
Local sensitivity analysis (OVAT), Global sensitivity analysis (GSA), Uncertainty quantification (UQ), Thermo-hydro-mechanical (THM), non-isothermal consolidation, Sobol indices

Nomenclature

Acronyms

Symbol	Description	Unit
GSA	Global sensitivity analysis	
MC	Monte Carlo	
OVAT	One variable at a time	

*Corresponding author
Email addresses:* aqeel.chaudhry@ifgt.tu-freiberg.de (Aqeel Afzal Chaudhry), joerg.buchwald@ufz.de (Jörg Buchwald), thomas.nagel@ifgt.tu-freiberg.de (Thomas Nagel)

SA   Sensitivity analyses

THM   Thermo-hydro-mechanical

UQ   Uncertainty quantification

Greek Symbols

Symbol	Description	Unit
α_{B}	Biot-Willis coefficient	$-$
β	Bulk compressibility of the mixture	Pa^{-1}
λ	Lamé parameter	Pa
μ_{w}	Dynamic viscosity of water	$\mathrm{Pa\,s}$
ν	Poisson's ratio	$-$
ϕ	Porosity	$-$
ρ_{s}	Intrinsic density of solid	$\mathrm{kg\,m}^{-3}$
ρ_{w}	Intrinsic density of water	$\mathrm{kg\,m}^{-3}$

Roman Symbols

Symbol	Description	Unit
$\mathbf{g}$	Gravitational acceleration vector	$\mathrm{m\,s}^{-2}$
a_{s}	Volumetric thermal expansion coefficient of solid	K^{-1}
a_{w}	Volumetric thermal expansion coefficient of water	K^{-1}
$c_{p,\mathrm{s}}$	Isobaric specific heat capacity of solid	$\mathrm{J\,kg}^{-1}\,\mathrm{K}^{-1}$
$c_{p,\mathrm{w}}$	Isobaric specific heat capacity of water	$\mathrm{J\,kg}^{-1}\,\mathrm{K}^{-1}$
E	Young's modulus	Pa
G	Shear modulus	Pa
K_{s}	Thermal conductivity of solid	$\mathrm{W\,m}^{-1}\,\mathrm{K}^{-1}$
k_{s}	Intrinsic permeability	m^2
K_{w}	Thermal conductivity of water	$\mathrm{W\,m}^{-1}\,\mathrm{K}^{-1}$

Subscripts

Symbol	Description	Unit
s	Solid	
w	Water	

1. Introduction

With the availability and continuous increase in computational resources, the tendency to employ increasingly complex mathematical models for decision-making, safety analysis and process understanding in various disciplines of science is becoming more prevalent. Among others, an important aspect of this increased complexity is the increased number of model inputs. When the models in question describe complex physical phenomena in the subsurface on large spatial and temporal scales, these parameters can usually not be determined without considerable uncertainty or imprecision. To understand how the uncertainty in the input parameters contributes to the uncertainty in the model output, sensitivity analyses are in use in medical science [1, 2, 3], earth and environmental science [4, 5, 6], chemical engineering [7, 8, 9], agriculture [10, 11, 12], oil and reservoir engineering [13, 14, 15] and others [16, 17, 18, 19]. One class of physical models with particular relevance to the geosciences are coupled thermo-hydro-mechanical (THM) models which are used for the assessment of nuclear waste disposal, geothermal energy exploitation, reservoir engineering and geotechnical engineering [20, 21, 22, 23, 24, 25, 26, 27, 28, 29, 30]. To better understand the dominant physical processes in subsurface engineering applications, their inherent uncertainties and the associated strategies for safety assessment of natural and engineered barriers, several long-term, large-scale in-situ experiments have produced a tremendous amount of valuable data over the past decades and continue to do so [20, 25, 31, 32, 33, 34, 35, 36, 37].

An assessment of different UQ and SA methods that work for coupled THM problems on an engineering scale is required for their reliable application to model-based decision making, optimization and (research) prioritization. Before proceeding any further, a clear distinction should be made between SA and UQ; while UQ revolves mainly around computing or quantifying the overall uncertainty in the model outputs, SA involves the relative attribution of said uncertainty to the uncertainty contributed by the various inputs [38]. The focus of the current paper is on the latter, while the topic of UQ is studied in a companion paper [1]. Of the analyses performed in the context of the mentioned applications, only a very small proportion of studies address aspects of uncertainties and sensitivities of the underlying coupled THM problems. Typically, sensitivity analyses of coupled THM problems remain local and are often done for the sake of completeness rather than for a comprehensive exploration of the parameter space. Even less is understood about the spatial and temporal variability of sensitivity measures. Some examples of UQ and/or SA of THM problems can be found in [39, 40, 41, 42, 43]. The most relevant work that we could find which addresses derivative-based local SA and variance-based GSA applied to a coupled THM numerical problem was by Nguyen et. al. [44] (without considering the spatio-temporal changes), but we could not find any work related to the SA of analytical THM model under study.

Due to different coupling levels (primary and secondary), non-linearities, and large system sizes numerical analyses of THM problems can be challenging. For an initial screening of available methods and interpretation of their results, it is therefore advantageous to have a well-understood analytical solution that nevertheless encompasses the most relevant primary couplings, can robustly cover the entire parameter space and remains computationally inexpensive. An analytical solution suitable for the purpose of this paper was provided by [45] and [46]; it describes consolidation around a point heat source located in a fully saturated isotropic elastic porous medium.

The objective of this paper is to systematically compare the information gained and conclusions supported by different approaches to sensitivity analysis: local (OVAT) and global sensitivity analysis (GSA) based on Sobol indices. The analyses were performed for different spatio-temporal settings to observe both near and far-field effects as well as early- and late-stage system response. We show which parameters and parameter interactions control the results in these different domains and provide physical interpretations. We provide application-oriented conclusions on the conditions which should be met when applying the different methods and examples for possible misinterpretations. The analysis results can furthermore serve as a benchmark case for SA software designed around coupled numerical simulators applied to THM problems.

The paper is organized as follows: Section 2 summarizes the analytical solution of the coupled THM problem under study. In Section 3, an initial screening of the input parameters by means of a classical local

---

[1]Currently under review

OVAT analysis is performed and its advantages and disadvantages for the case under study are discussed. Sections 4 and 5 discuss the results of an extended full-range local sensitivity analysis and global sensitivity analysis (GSA), respectively. Section 6 contains the concluding remarks. Generally, the paper follows the natural workflow and complexity of sensitivity analyses and therefore, each section contains all relevant details and corresponding results. The physical interpretation of the results is only discussed in detail in the Section 5 to avoid repetitions. In our wording we try to stick to terms familiar to the engineering community as much as possible.

2. The THM model: non-isothermal consolidation around a point heat source

2.1. Description of the physical model

The sensitivity analyses of a THM problem are performed on the analytical solution of non-isothermal consolidation around a point heat source embedded in a fully saturated porous medium. As is common for THM problems, the model is controlled by the three independent variables temperature T, pore-pressure p and displacement of the solid skeleton $\mathbf{u}$. A change in temperature caused by the heat source induces a response from the solid skeleton and the pore fluid at different time scales resulting in a pressure gradient that drives the flow of fluid away from the source causing the porous medium around the heat source to undergo a transient deformation. Fluid flow induced by the resulting pressure gradient diminishes with the passage of time depending on location as a local steady-state is reached. In the context of radioactive waste disposal, the coupled THM model mimics a disposal cell emitting decay heat embedded in a fluid-saturated rock type such as clay rock.

For the details related to the derivation of the analytical solution, the reader is referred to [45] and [46]. Here, we simply summarize the relevant equations.

The thermal part in this case is based on a heat balance equation which is given as [47]

$$(\rho c_p)^{\text{eff}} \dot{T} + \rho_{\text{w}} c_{p,\text{w}} \operatorname{grad} T \cdot \mathbf{v} - \operatorname{div}(K \operatorname{grad} T) = q_T \tag{1}$$

where q_T is a heat source per unit volume and the heat capacity $(\rho c_p)^{\text{eff}}$, heat conductivity K and Darcy velocity $\mathbf{v}$ are given as

$$(\rho c_p)^{\text{eff}} = \phi \rho_{\text{w}} c_{p,\text{w}} + (1 - \phi) \rho_{\text{s}} c_{p,\text{s}} \tag{2}$$

$$K = \phi K_{\text{w}} + (1 - \phi) K_{\text{s}} \tag{3}$$

$$\mathbf{v} = -\frac{k_{\text{s}}}{\mu_{\text{w}}} (\operatorname{grad} p - \rho_{\text{w}} \mathbf{g}) \tag{4}$$

The hydraulic part is based on the mass balance equation which is given as

$$\beta \dot{p} - [\phi a_{\text{w}} + (1 - \phi) a_{\text{s}}] \dot{T} + \alpha_{\text{B}} \operatorname{div} \dot{\mathbf{u}} + \operatorname{div} \mathbf{v} = q_{\text{H}} \tag{5}$$

The mechanical part is based on the quasi-static balance of linear momentum of the mixture and is given as

$$\operatorname{div} \boldsymbol{\sigma} + \rho \mathbf{g} = \mathbf{0} \tag{6}$$

where $\rho = \phi \rho_{\text{w}} + (1 - \phi) \rho_{\text{s}}$ and $\boldsymbol{\sigma}$ is the total stress given as

$$\boldsymbol{\sigma} = \boldsymbol{\sigma}' - \alpha_{\text{B}} p \mathbf{1} \tag{7}$$

where $\mathbf{1}$ is the second-order identity tensor and $\boldsymbol{\sigma}'$ is the effective stress tensor for which we assume a linear elastic and isotropic behaviour:

$$\boldsymbol{\sigma}' = 2G \boldsymbol{\varepsilon}^{\text{el}} + \lambda \operatorname{tr} \boldsymbol{\varepsilon}^{\text{el}} \mathbf{1} \tag{8}$$

where elastic strain $\boldsymbol{\varepsilon}^{\text{el}}$ is related to the total strain $\boldsymbol{\varepsilon}$ as

$$\boldsymbol{\varepsilon}^{\text{el}} = \boldsymbol{\varepsilon} - \frac{a_{\text{s}}}{3} \Delta T \mathbf{1} \tag{9}$$

4

The analytical solution [45, 46] solves this set of equations for spherical symmetry and a constant heat flux emitted at the center of the domain in a domain with homogeneous initial conditions. The assumptions made while deriving the analytical solution also underlay this work and can be stated as follows; no advection is considered, so the second term on the left hand side of Eq. (1) vanishes. The energy balance thus becomes uni-laterally coupled to the HM-part of the model and validity is limited to low-permeable media. This is the type of medium in which thermal fluid pressurization is most pronounced. Also, the gravitational force is neglected and assumed to be accounted for in the initial stress and pore-pressure fields, so the last term on the right hand side of Eq. (4) and the left hand side of Eq. (6) vanishes. The solid and fluid phases are both assumed to be intrinsically incompressible, which results in $\alpha_B = 1$ and $\beta = 0$. As a consequence, the density change of a phase is caused only by the change in temperature. This assumption usually leads to conservative estimates of thermal pressurization. No external fluid source or sink is present i.e. $q_H = 0$. Mechanical, thermal and hydraulic isotropy are assumptions already intrinsic to the above equations. Solution for T and p follows from Eqs. (23) and (24) in [46], respectively. It should be noted here that the values of T and p in the results refer to the values above the reference values (initial conditions). Furthermore, since the THM problem under study possesses spherical symmetry, the solution for displacement follows from Eq. (30) in [46].

2.2. Input parameters and their variability

Table 1: Input parameters for sensitivity analysis. Data based on [36, 48].

Parameter	Symbol/Unit	Min	Max	Mean	Std. Dev.	Distribution
Total thermal conductivity	K / $\mathrm{W\,m^{-1}\,K^{-1}}$	1.29	2.45	1.79	0.34	Truncated normal
Total specific heat capacity	C / $\mathrm{J\,kg^{-1}\,K^{-1}}$	774	1182	978	68	Normal
Total density	ρ / $\mathrm{kg\,m^{-3}}$	2420	2540	2480	30	Truncated normal
Young's modulus	E / Pa	$5.5 \cdot 10^9$	$20.1 \cdot 10^9$	$12.8 \cdot 10^9$	$3.7 \cdot 10^9$	Truncated normal
Volumetric thermal expansion coefficient of solid skeleton	a_s / $\mathrm{K^{-1}}$	$3 \cdot 10^{-5}$	$7.5 \cdot 10^{-5}$	$5.25 \cdot 10^{-5}$	-	Uniform
Intrinsic permeability	k_s / $\mathrm{m^2}$	$7.8 \cdot 10^{-21}$	$2.2 \cdot 10^{-19}$	$5.6 \cdot 10^{-20}$	$5.5 \cdot 10^{-20}$	Truncated normal
Poisson's ratio	ν / $-$	0.2	0.4	0.3	$-$	Triangular
Porosity	ϕ / $-$	0.097	0.185	0.15	0.0276	Truncated normal

Instead of simply varying all the model parameters by a given percentage above and below certain base values, we used data from in-situ experiments on Callovo-Oxfordian (COx) clay rock to specify variability [36, 48]. The experimental data is available in the form of various types of distributions where mean, standard deviation, variation range and type of distribution are specified in each case. We chose 8 of these parameters which are listed in Tab. 1 to be used as input variables for SA. It is worth mentioning that in the data available at hand, the density and specific heat capacity of the mixture are given. In the sequel, we will use C instead of c_p for convenience. The strength of the heat source is chosen to be 3 kW. The values of the parameters that are not explicitly mentioned here, are taken from [46]. Fig. 1 shows the corresponding probability density functions (PDF) and cumulative distribution functions (CDF) for these parameters.

The SA is performed for different spatio-temporal settings to observe, relatively speaking, near and far-field effects as well as early- and late-stage system response. The values of radii and times chosen for the analysis are combinations $r \times t$ of the sets

$$r \in \{r_1, \ldots, r_{10}\} = \{2\,\mathrm{m}, 4\,\mathrm{m}, 6\,\mathrm{m}, 8\,\mathrm{m}, 10\,\mathrm{m}, 12\,\mathrm{m}, 15\,\mathrm{m}, 20\,\mathrm{m}, 25\,\mathrm{m}, 30\,\mathrm{m}\} \tag{10}$$

$$t \in \{t_1, \ldots, t_{10}\} = \{1\,\mathrm{d}, 7\,\mathrm{d}, 30\,\mathrm{d}, 90\,\mathrm{d}, 180\,\mathrm{d}, 1\,\mathrm{y}, 2\,\mathrm{y}, 3\,\mathrm{y}, 4\,\mathrm{y}, 5\,\mathrm{y}\} \tag{11}$$

In the sequel, the subscripts of r & t will refer to their corresponding values mentioned above, e.g. $t_7 = 2\,\mathrm{y}$. Figs. 2a, 2b and 2c show the analytical solution for T, p and u_r for the minimum, mean and maximum values of the input parameters, respectively, as defined in Tab. 1. Apparently, one observes that a collective increase in parameter values from lower to mean and subsequently to upper bounds results in a decrease in T and u_r at r_1 but this is not the case with p where the maximum value of p is observed for mean values
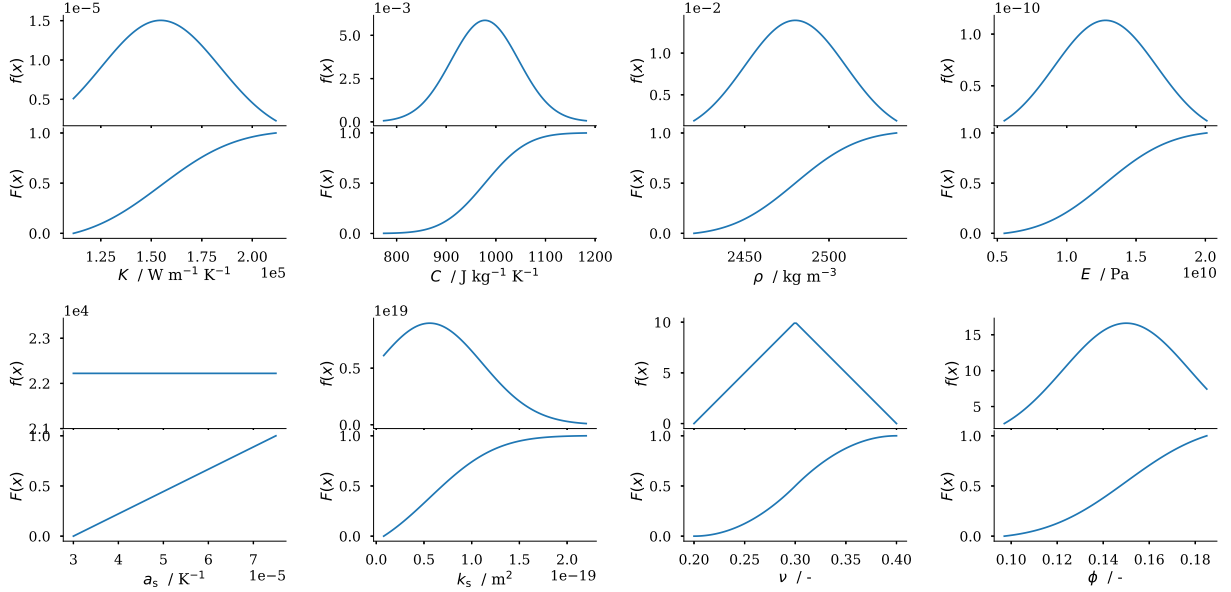
Figure 1: A priori probability density function (PDF) $f(x)$ and cumulative distribution function (CDF) $F(x)$ for input variables according to Tab. 1.

of input parameters. This observation is quite qualitative in nature and it is too early to conclude anything at this stage, but it may present a first indication of a relatively complex and non-intuitive behaviour of p compared to T and u_r. We will return to this observation later.

3. Initial OVAT screening

Local sensitivity analysis is commonly referred to as one-variable-at–time (OVAT), one-function-at-time (OFAT) or univariate sensitivity analysis. The computational cost of a comprehensive sensitivity analysis increases significantly with the number of input parameters. Thus, before performing an extensive SA, an initial screening can be helpful to simplify the model by eliminating input parameters deemed insignificant. One such screening method uses the so-called Tornado charts. To draw a Tornado chart, first a base value for all input parameters is chosen. As an example, the base values can either be the best known values for the model under consideration or the mean values if the input parameters are available in form of some range (case under study). The base values are then increased and decreased either uniformly by a certain percentage or to maximum and minimum values of the input parameters. For every input parameter, the difference in model output for minimum, base and maximum values of input parameters is then plotted in form of bars with the width of bars decreasing from top to bottom, thus giving it the shape of a Tornado. The width of the bars is thus a direct indicator of the significance of a certain input parameter. Thus an input parameter with no or a relatively small contribution in a Tornado chart can be excluded from more extensive sensitivity analysis or uncertainty quantification, especially if the computational resources available at hand are limited. The threshold value for insignificance is typically at the discretion of the modeller and requires physical insight. It is important to note here that it is a common practice to plot both sides of the bars (left and right side of base values) in a Tornado chart with different colors to show direct and inverse relation between input and output. Thus, in our case, a blue color on left side and a red color on right side will indicate that an increase (decrease) in input parameter will result in an increase (decrease) in the output and vice versa. Fig. 3a shows such a Tornado chart for the analytical solution at a point 2 m from the heat source after 7 days, where the base values are chosen to be the mean values and bounds as the maximum and minimum values of input parameters from Tab. 1. It can be observed that temperature is
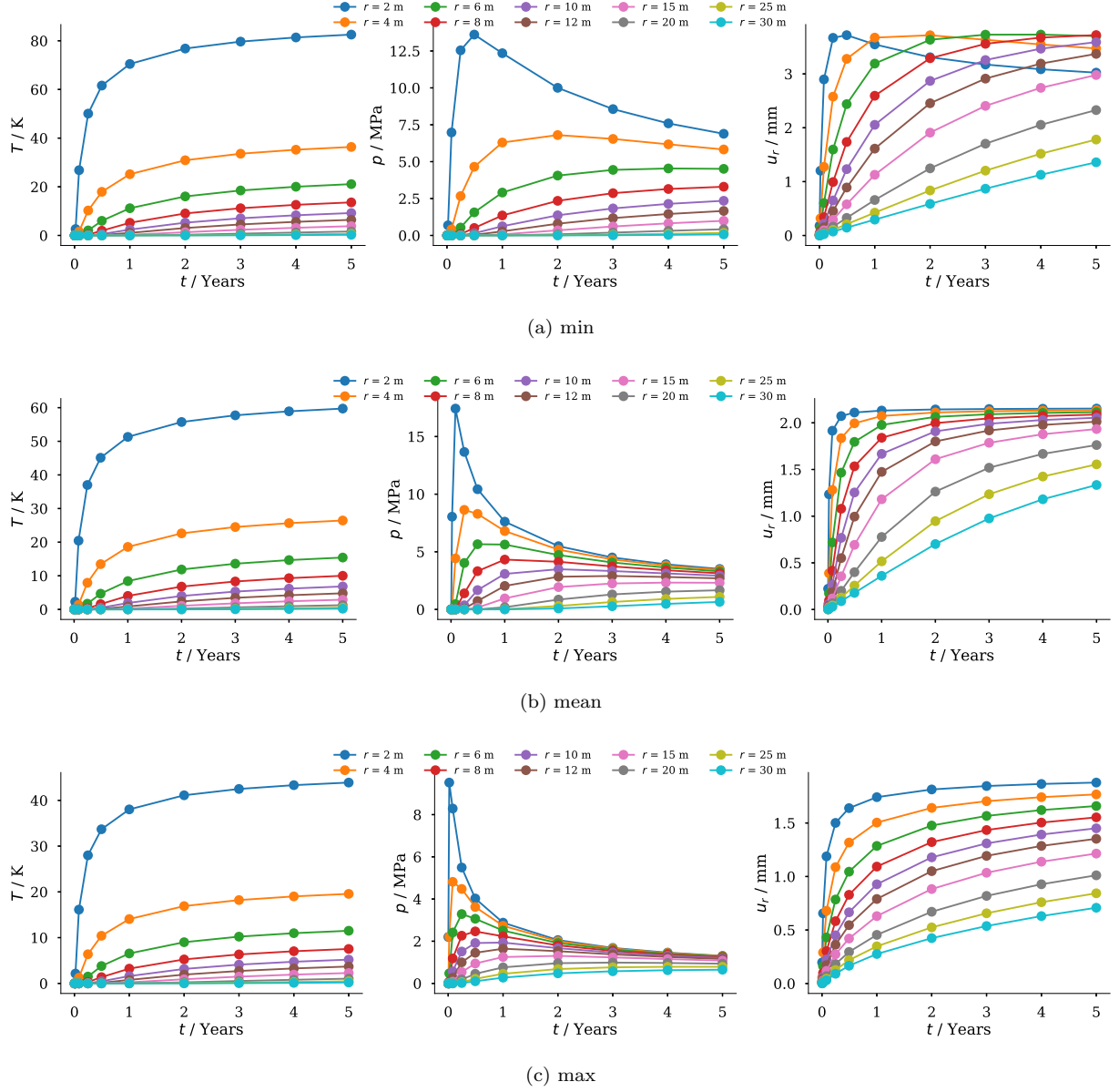
6

Figure 2: Analytical solution at $t \in [t_1, t_{10}]$ at $r \in \{r_1, \ldots, r_{10}\}$ for parameter settings 'min', 'mean' and 'max' as given in Tab. 1.

sensitive to C, K and ρ in descending order while insensitive to all other input parameters. In contrast, the number of sensitive parameters for pressure and displacement is larger and one may conclude that pressure is most and least sensitive to E & ρ, while displacement to k_{s} & ρ, respectively. But, the question arises; are the above conclusions safe to be made? Since the analytical solution under study is known to vary with time as well as distance from the heat source, the above conclusions can only be regarded as preliminary at this stage. Fig. 3b shows the Tornado chart for all output variables at a distance of $2\,\mathrm{m}$ after 90 days. It can be observed that at this later time point, temperature appears to become more sensitive to K than C in this case which is in contrast to the observation made earlier. Furthermore, pressure now appears to be most

sensitive to k_s[2] instead of E, and E which appeared to be on the top in the Tornado chart after 7 days, now ranks fifth after 90 days. Also the sensitivity to the remaining parameters appears to be different. In case of displacement after 90 days, although k_s and ρ still appear to be most and least significant parameters, the sensitivity ranking of the remaining parameters has changed. A more careful look at both Tornado charts also shows that at $t = 7\,\mathrm{d}$ (Fig. 3a), u_r decreases with an increase in ν (red color bar on left) which is not the case at $t = 90\,\mathrm{d}$ (Fig. 3b). One can also observe the shift in both base-line values and spread due to the transient development of the process.

Even at the so-called screening stage, one may be interested to see if there are non-linearities present. Tornado charts may give a slight hint of non-linear behaviour, provided the base values and the average of upper and lower bounds of input parameters are equal, which is the case with C, ρ, E, a_s and ν. In such a case, an unequal width of bars on left and right side of the base line may indicate that input parameter and output are non-linearly related. From Fig. 3a & Fig. 3b, it appears that p and u_r may depend only linearly on a_s. It is also worth mentioning that in case of C-T in Fig. 3b, a slightly different value of r or t might have led to equal width of red and blue bars indicating falsely a linear relation. Another important aspect to notice is k_s-p in Fig. 3a where both red and blue bars appear on the same side of the base line which is not the case in Fig. 3b. This can be an indication of a transition from inverse relation to direct relation or vice versa (non-monotonic relation). We will attempt to verify some of these observations in the next section.
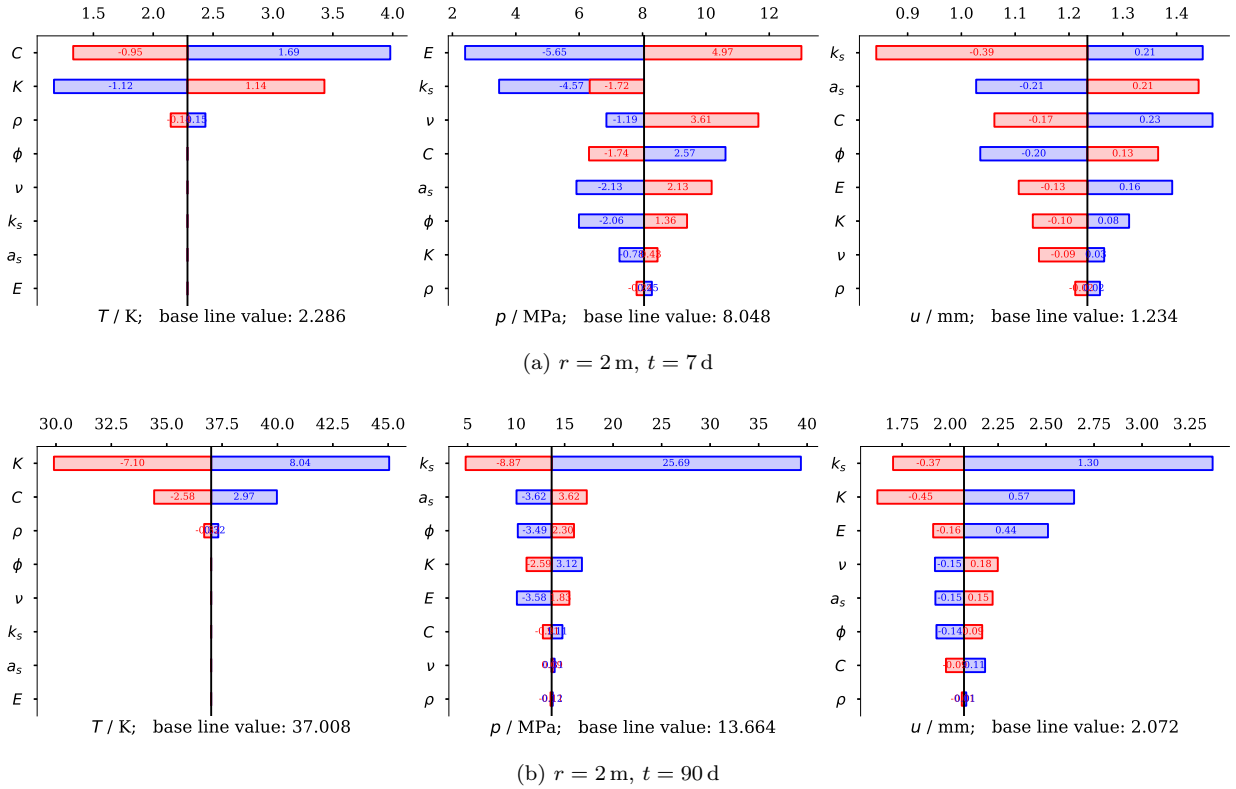

Figure 3: Tornado chart for temperature, pressure and displacement close to the heat source at different time points.

---

[2]We comment on the asymmetry later.

4. Full-range local sensitivity analysis (OVAT)

It is not uncommon in the literature to consider the sensitivity analysis of a given problem finished based on the result in the previous section, i.e. a simple up or down regulation of individual input parameters. Although the Tornado charts are quite efficient when it comes to computational cost (only 3 computations per input parameter), care should be taken as a Tornado chart only gives the output points for the specified limiting and central values of the input parameters and does not provide any reliable information of their effect between these values. Neither can these values be considered bounds which is often overlooked based on an intuition biased towards linearity. As mentioned in the previous section, a relatively better understanding of the parameter sensitivity can be achieved by a multi-point local sensitivity analysis. Similar to the classical OVAT analysis, first an upper and lower limit is chosen for each input parameter. Then in contrast to the Tornado charts presented above, the input parameter is varied in small intervals between these limits while keeping all other parameters fixed. This process is then repeated for all input parameters. Naturally, a higher number of subdivisions will give a better understanding of local sensitivity and non-linearity over the entire parameter range, but comes at the expense of a higher computational cost. Depending on the degree of non-linearity, the number of subdivisions need not be very high in most practical cases. In the present case, of course, computational cost is of no concern.

Fig. 4 shows the OVAT analysis at $r = 2\,\text{m}$, $t = 7\,\text{d}$ for 100 subdivisions. The red and blue boxes are spanned by the input and output variation computed in the Tornado charts (Fig. 3a). It is appropriate to mention here that it is not a common practice to draw such boxes in OVAT charts. It was done here intentionally for comparison purposes in order to show where information from Tornado charts may fail to provide a complete picture. The input parameters contributing most and least to the outputs are plotted from top to bottom. Evidently, the OVAT chart in Fig. 4 gives a better insight into the non-linearities present in the model in comparison to the Tornado chart in Fig. 3a. Before proceeding further, we try to verify the specific test case observations made at the screening stage for which we also perform the OVAT analysis at $r = 2\,\text{m}$, $t = 90\,\text{d}$, the result of which is shown in Fig. 5. Here we see again in both figures that T is sensitive to K, C & ρ only and that the sensitivity of T to K & C is reversed between Fig. 4 & Fig. 5. But, in case of p, for the specified bounds of k_s, the maximum value of p obtained by the full-range OVAT analysis (Fig. 4) is higher than that obtained in the Tornado chart as seen in Fig. 3a. This shows that it is quite possible that a Tornado chart does not provide bounds of the model output leading to unreliability when it comes to decision making based on extreme values. In other words, conservative inputs do not necessarily lead to conservative estimates of outputs. This effect can also be observed in case of ν-p in Fig. 5. The OVAT analysis in Fig. 4 & Fig. 5 shows that all the parameters except a_s involved in this study show non-linear behaviour to some extent and that the sensitivity varies with time even at a given distance from the heat source.

Even in case of a_s, one cannot say with utmost certainty, that it will be linear for all combinations of r and t, and thus it is important to also have a detailed look on the spatio-temporal changes in parameter sensitivity. One way of doing this, is to perform the OVAT analysis for a certain input parameter and a certain output for all permutations of r and t within the intervals defined above. For this purpose, we choose all combinations of $r_1 - r_5$ and $t_1 - t_5$. Only selective sets of input-output are shown here which appeared to be of particular interest.

Fig. 6 shows the results of the OVAT analysis for T vs K. It can be observed that at (r_1, t_2), an increase in K resulted in a small increase in temperature but this effect is reversed after the first week of heating. This effect is visible at all distances from the heat source as soon as the temperature signal initially arrives at these distances. A similar effect can also be observed in case of p vs k_s in Fig. 7 where an increase in intrinsic permeability will result in higher pore pressures initially but this effect is reversed sooner than in case of K vs T. Also, the relation between k_s & p appears to be highly non-linear for very small values of intrinsic permeability. A summary of the type of relationship observed between input parameters and model outputs by considering all possible combinations of r and t under study, is given in Tab. 2.

We have so far examined two different ways of looking at the OVAT results: first, by fixing r & t while considering all input parameters and model outputs in a single plot with sensitivity descending from top to bottom of the chart (Fig. 5, Fig. 4); and second, by fixing a single input parameter as well as a single

model output while considering all possible combinations of r & t under study (Fig. 6, Fig. 7) in order to examine spatio-temporal sensitivity variations. Both types appear to have advantages and disadvantages in communicating particular features of the problem: The former allow one to observe the sensitivity of parameters in comparison to each other; the latter give an impression of how the effect of a parameter varies with the location of an observation point as well as over time. This demonstrates that sensitivities are not invariant quantities. In other words, it matters where and when one measures if a certain effect is to be observed.

For interpreting the significance of an observation, e.g. a particularly strong non-linearity, it is furthermore important to take a look at the scale of the abscissa of the graphs: the strongest non-linearities occur in combination with the non-monotonic behaviour, i.e. the switch from direct to inverse parameter sensitivity. As such, while strongly non-linear, the actual sensitivity measured in terms of the range of the observed quantity (e.g. temperature) is low at this combination of r and t. This is often, but not always the case.

There are some major shortcomings of the local sensitivity analysis in general. Primarily, it cannot account for interactions between input parameters. Another major drawback of OVAT analysis is that it does not cover the whole parameter space, the so-called curse of dimensionality [49]. Imagining a simple example of a cube which spans the space of three input parameters, the OVAT analysis will cover only the parameter values lying on the axes inside the cube which will lead to the underestimation of the response surface bounds. This leads us to the need for global sensitivity analysis which is performed in the next section. Modifications of the OVAT approach where the analysis is repeated around different sets of baseline values in order to better capture the parameter space and get an impression of parameter interactions can be considered a special case of or transition to GSA.

Table 2: Summary of parameter behaviour observed by OVAT analysis. "Non-monotonic" means that the parameter sensitivity reversed from direct to inverse for some combinations of r & t

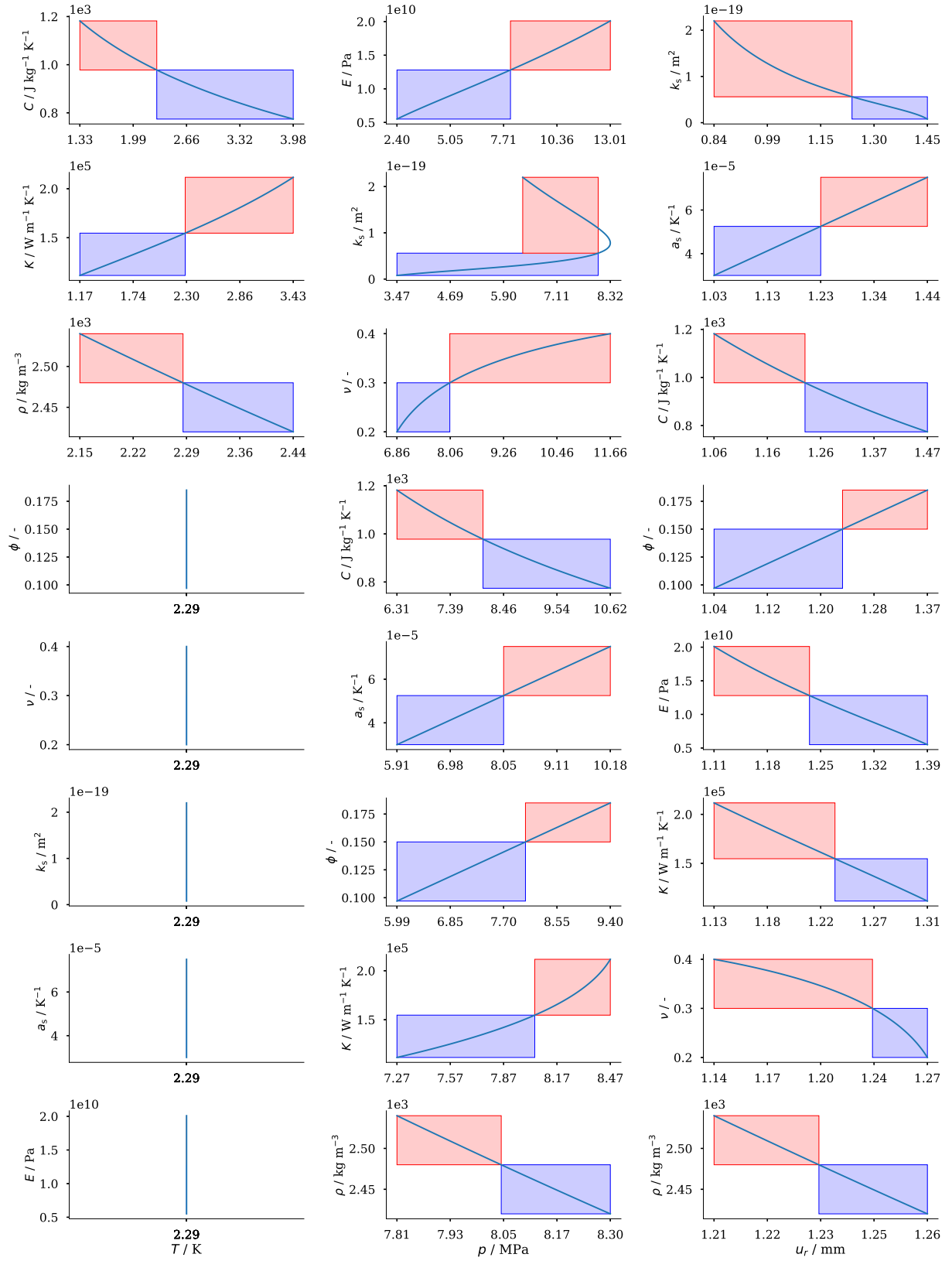|	K	C	ρ	E	a_s	k_s	ν	ϕ
T	Non-monotonic	Inverse	Inverse					
p	Non-monotonic	Inverse	Inverse	Direct	Direct	Non-monotonic	Non-monotonic	Direct
u	Inverse	Inverse	Inverse	Inverse	Direct	Inverse	Non-monotonic	Direct

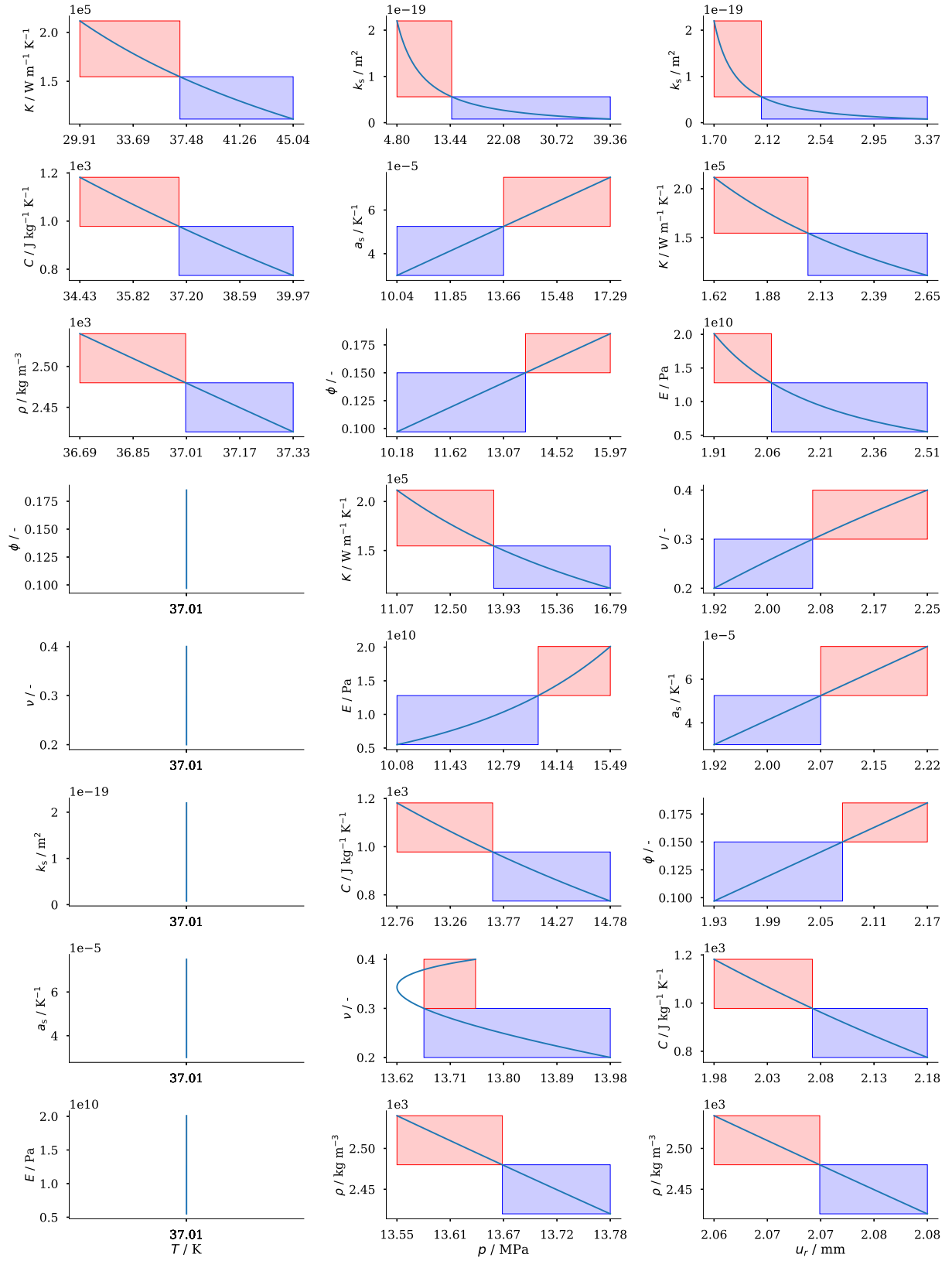Figure 4: OVAT analysis at $r = 12$ m, $t = 7$ d for all model outputs

Figure 5: OVAT analysis at $r = 12\,\text{m}$, $t = 90\,\text{d}$ for all model outputs
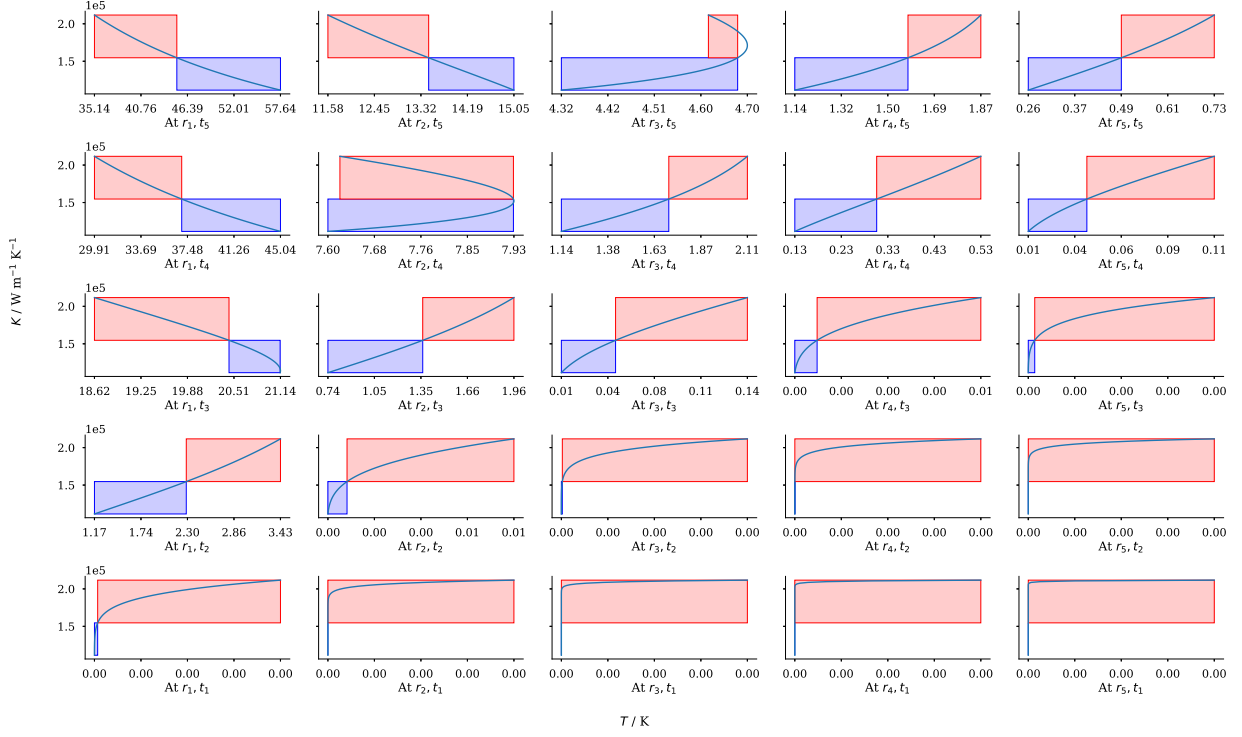
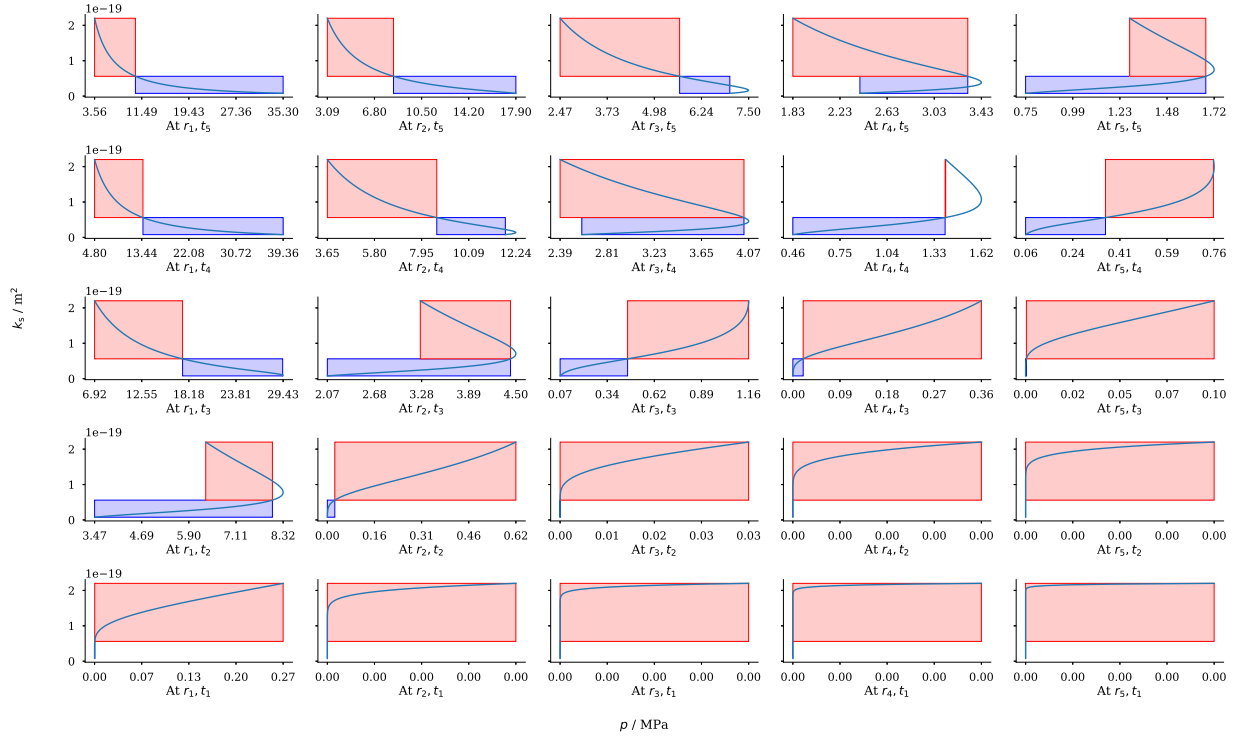Figure 6: OVAT analysis for model input K and output T

Figure 7: OVAT analysis for model input k_s and output p

13

5. Global sensitivity analysis (ANOVA)

5.1. Preliminary remarks and Sobol indices

Global sensitivity analysis aims at calculating sensitivity measures that represent the system behaviour over the entire parameter space. Some of the common types of GSA in use are the method of Morris, also called elementary effects method (EEM) [50, 51] (used mainly for screening purposes), the Delta moment independent measure [52], or the derivative-based global sensitivity measure (DGSM) [53]. However, the most common among these are the variance-based GSA techniques. Two frequent types of variance-based GSA, also referred to as ANOVA (Analysis of variance) in use are the Fourier amplitude analysis test (FAST) [54] and Sobol's sensitivity analysis [55]. In this work, we restrict ourselves to Sobol's sensitivity analysis while discussion about its comparison with FAST can be found in the literature [56]. Major advantages of Sobol analysis over FAST include its relatively straightforward implementation, higher accuracy and the ability to address higher order interactions.

Sensitivity analysis refers to the study of how different sources of uncertainty in the model input contribute to the uncertainty in the model output [57]. In the current work, we restrict ourselves to first and second-order sensitivity indices which are written as

$$S_i = \frac{V_i(Y)}{V(Y)} \quad , \quad S_{ij|_{i \neq j}} = \frac{V_{ij}(Y)}{V(Y)} \tag{12}$$

The first-order index S_i is thus a measure of the partial variance contributed by a single parameter i to the overall variance in the response variable, while the second-order index gives a measure of the partial variance contributed by the interaction of two parameters i, j to the overall variance. Further details can be found in Appendix A. Another important measure of the sensitivity index of an input parameter is the total effect index or total order index which is the sum of a parameter's first or main-order index and its higher-order interactions with other input parameters, i.e.

$$S_{\mathrm{T}\,i} = S_i + \sum S_{ij} + \sum S_{ij...n} \tag{13}$$

This index becomes particularly useful in cases where one wants to avoid the explicit computation of individual interactions due to high computational costs (e.g. for initial screening) as $S_{\mathrm{T}\,i} = S_i$ will indicate the absence of parameter interactions (additive models) while $S_{\mathrm{T}\,i} > S_i$ will indicate otherwise. It should be noted here that $\sum_i S_{\mathrm{T}\,i}$ can be greater than 1 because S_{ij} is accounted for twice in $S_{\mathrm{T}\,i}$. In other words, assuming an example where only second-order interactions are present, one may write $\sum_i S_{\mathrm{T}\,i} - \sum_i \sum_j S_{ij} = \sum_i S_i + \sum_i \sum_j S_{ij} = 1$ [58].

As seen from the definitions in Appendix A, S_i measures the relative variance that could be reduced if X_i could be fixed to a single value, while $S_{\mathrm{T}\,i}$ measures the relative variance that would be left if all factors but X_i could be fixed [59].

The numerical computation of the indices is described in Appendix B.

5.2. Analysis of the point heat source THM problem

5.2.1. General screening

We used 100 000 samples which resulted in 1 800 000 re-evaluations of the model for a single pair of (r, t). It is worth mentioning here that we chose such high number of samples based on convergence of confidence bounds and because computational effort was of no concern for the model studied. Keeping in mind that this will change drastically for numerical models, we investigated the results by using one order of magnitude lower sample numbers, the results of which are provided as a supplement with this work. The analysis was carried out for the 100 pairs of $r \times t$ defined previously. Fig. 8 shows a stacked bar chart of S_i and $S_{\mathrm{T}\,i}$ for T, p and u_r at r_1 and t_2-t_4. It should be noted that it is a common practice to plot a bar chart where S_i and $S_{\mathrm{T}\,i}$ are plotted next to each other, hence an equal height of bars will indicate the absence of interactions for that particular input parameter. We chose to plot the stacked version to also incorporate the effect of change in r or t in the same chart. As seen earlier at the screening and full-range OVAT stages, T appears
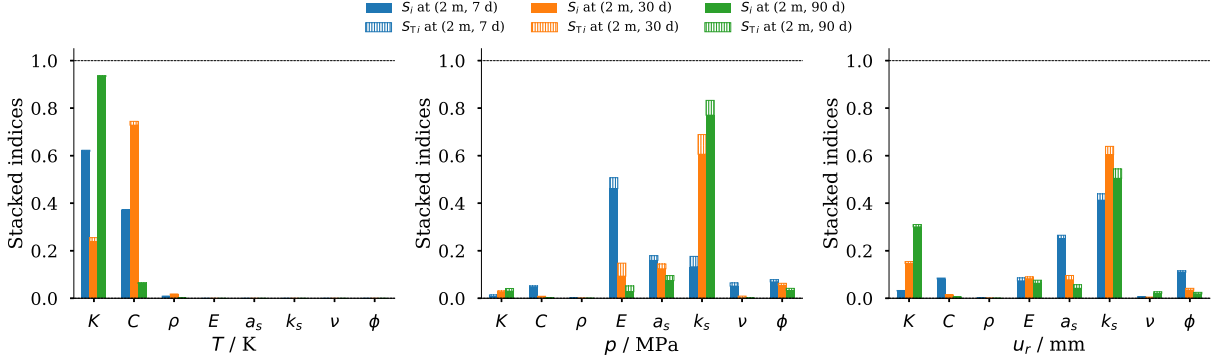
Figure 8: Stacked bar chart for S_i and $S_{\mathrm{T}\,i}$ at fixed distance r_1 and times t_2-t_4
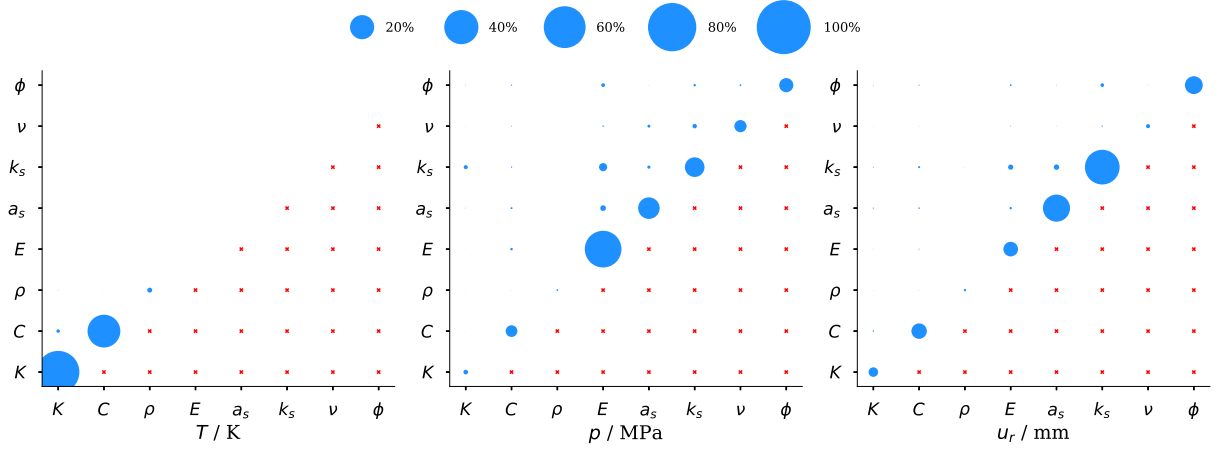

Figure 9: Chart for S_i and S_{ij} at r_1 and t_2. Circles along the diagonal represent S_i while off-diagonal entities (except crosses) show interactions. The graph is symmetric, so only the upper triangle is filled. The areas of the circle are proportional to the magnitude of the sensitivity index.

to be sensitive to K, C and very slightly to ρ but what is interesting to see is that the temporal change in sensitivity of both K and C is not monotonic. This is also in line with previous observations and points to a spatio-temporal variation of certain parameter sensitivities associated with the ongoing processes of heat and mass transport as well as deformation. To investigate this further, we plot spatio-temporal sensitivity maps (Figs. 10 to 15).

The relative impact of parameter interactions can be studied by plotting a chart such as Fig. 9 which shows S_i and S_{ij} at r_1 and t_2. Dots along the diagonal represent S_i while off-diagonal entities (except crosses below the diagonal) show interactions. This allows one to gain a fast and intuitive overview over the relative magnitude of first- and second-order indices.

5.3. Spatio-temporal sensitivity maps—temperature

In these graphs, each box shows the sensitivity index for a specific combination of r and t where change in color in horizontal and vertical direction shows the corresponding change in sensitivity w.r.t spatial and temporal domains, respectively. Figs. 10 and 11 present S_i and S_{ij} for T, respectively, for all combinations of r and t. Again, it is evident that T is sensitive to K and C which also makes sense from a physical perspective. But in contrast to the OVAT screening results (e.g. Fig. 3a), the sensitivity to ρ seems far less pronounced here. One possible reason for this might be, since in the OVAT analysis, outputs are not normalized, thus
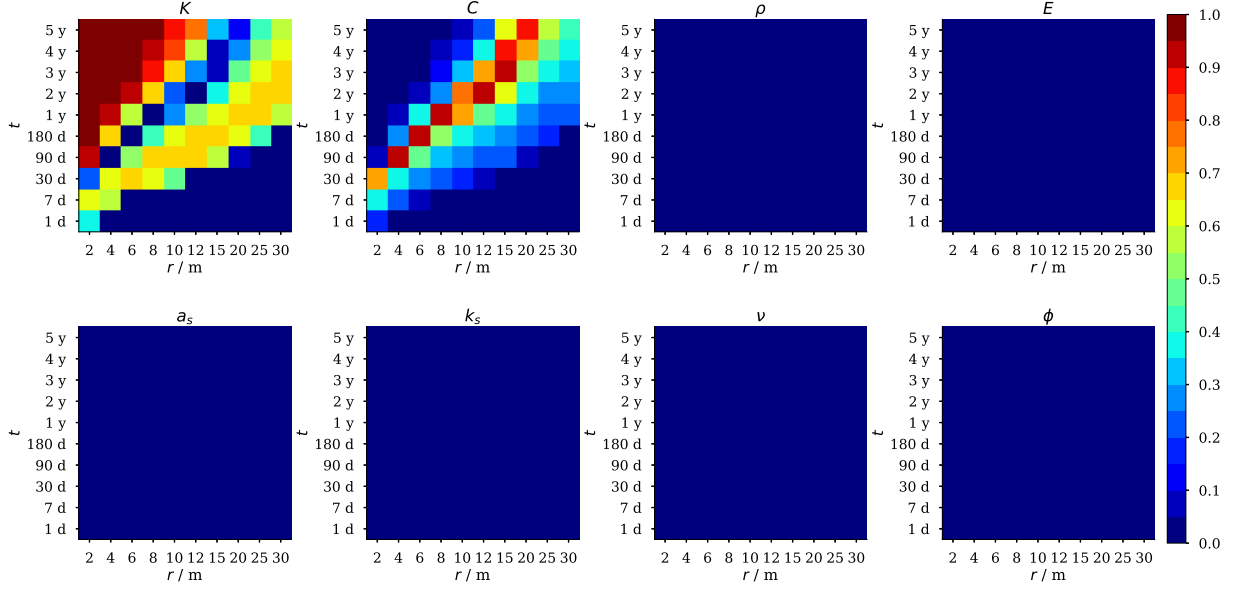
15

Figure 10: S_i for T for all combinations of r and t.

while comparing the width of the bars of K, C and ρ in Tornado chart (Fig. 3a), the comparative sensitivity to ρ appeared more pronounced. But if we carefully look at the variation of temperature produced by K and C in Fig. 3a (less than 3 K), it is very small in comparison to the overall variation observed for parameter combinations (above 80 K) shown in Fig. 2a. Since the GSA covers the entire parameter space instead of relying on the minimum, mean or maximum values, it provides a more representative picture than the OVAT analysis. Thus, we may safely conclude from GSA results for temperature that sensitivity of temperature predictions to ρ is of very little significance (overall maximum value of $S_i = 0.022$). Generally, this is only true for the data at hand where the percentage of uncertainty in input data for ρ is small in comparison to the uncertainty of K and C. The sensitivity maps also recover the non-monotonous trends observed earlier: one observes a decrease in sensitivity to K which later increases again and then remains high permanently (left most column in Fig. 10). In case of C, we also observe this non-monotonous behaviour but in a fashion completely complementary to the behaviour of K: the sensitivity first increases and then decreases which ultimately ends in T not being sensitive to C at all. This transition of sensitivity between K & C occurs earlier in the near field and later in the far field and the transition region widens diffusively (the sandwiched blue and red diagonal for K & C in Fig. 10 widens while moving from left to right, even though the time difference is in years). This behaviour can be explained physically: before the arrival of the temperature front, neither of the thermal parameters play an important role. During the passage of the temperature front the temperature rate is determined strongly by the material's heat capacity C controlling the transient part of Eq. (1). Once the front has passed, the remaining temperature gradient is determined by the stationary part of Eq. (1) and thus by the material's heat conductivity. The actual arrival time is determined by the heat diffusivity which is a combination of both parameters. This parameter interaction is picked up by the second-order indices, as evidenced by Fig. 11 which shows that interactions are present in case of temperature for the case of K & C especially at earlier times when the temperature signal arrives at a given location. The unilateral thermal coupling to the hydraulic and mechanical parts (Eq. 1), explains the insensitivity of temperature to parameters like E or k_s (no advection). If the range of uncertainty in the data for ρ were wider, we would have expected that sensitivity for ρ-T will follow somewhat a similar pattern as C-T.
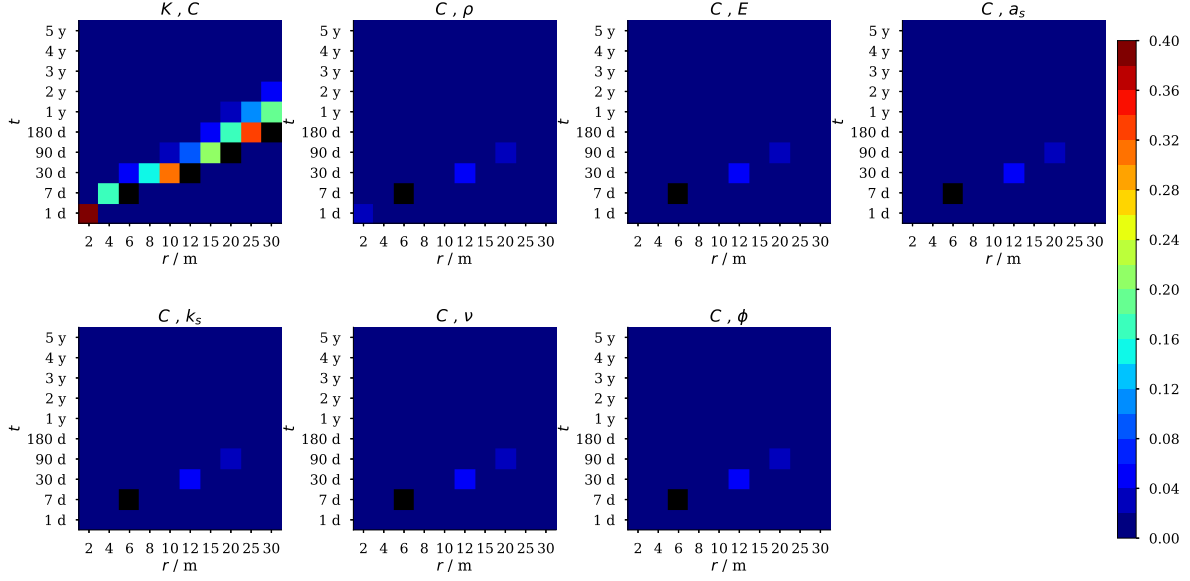
16

Figure 11: S_{ij} for T for all combinations of r and t.

5.3.1. Confidence bounds on higher-order indices

When it comes to the accuracy of the computed indices, we observed that these early arrival areas need special attention. For example, the blue colored boxes in the lower right regions of K-T and C-T in Fig. 10 are the regions where no parameter combinations produced any output T, but at the very next value of time, a small percentage of combinations of input parameters produced very small values of temperature change. During the computation of the sensitivity indices, such circumstances created a sort of numerical noise and produced unrealistically high values of sensitivity indices. The confidence intervals associated with these predictions where likewise unacceptably high (data not shown). To avoid unphysical sensitivity indices, confidence intervals spanned by $\pm 5\%$ were applied as a filter and the values outside these bounds are shown with black color, cf. Fig. 11. To verify if these unrealistically high values can indeed be attributed to the computational scheme, we tested it using the commonly used test of Ishigami's function (mentioned earlier) and found out that in the case where parameter interactions are involved, even extremely high sample numbers still resulted in either negative values of sensitivity indices or sensitivity indices being very small in comparison to the confidence bounds. It should be noted though that this numerical noise does not influence the understanding of the results if the sample size is large enough and if proper filtering is employed. Nevertheless, physical understanding should always be used to check the plausibility of the obtained results. With these considerations, T is seen to be primarily sensitive to K and C, and their interaction is particularly relevant for the speed at which the temperature signal travels, Fig. 11.

5.4. Spatio-temporal sensitivity maps—pressure

Figs. 12 and 13 show spatio-temporal maps for S_i and S_{ij} with respect to pressure. Sensitivity of pressure is most pronounced[3] to k_s, E and a_s. Qualitatively, k_s-p follows a similar trend as observed in case of K-T while E, ν and ϕ appear to be significant in the zone where the pressure front first arrives. Sensitivity of p to a_s is again more pronounced in near field at earlier times but does not fade away quite as much as in case of E, ν and ϕ as time passes. Fig. 13 shows the significance of parameter interactions in case of pressure and suggests that interactions $E - k_s$ and $k_s - \nu$ are the most prominent ones.

---

[3]Note that small sensitivies are not shown due to the discrete color scheme used. For example, K has an overall maximum value of $S_i = 0.03$ and C of $S_i = 0.047$, which is just below the threshold for visibility of 0.05.
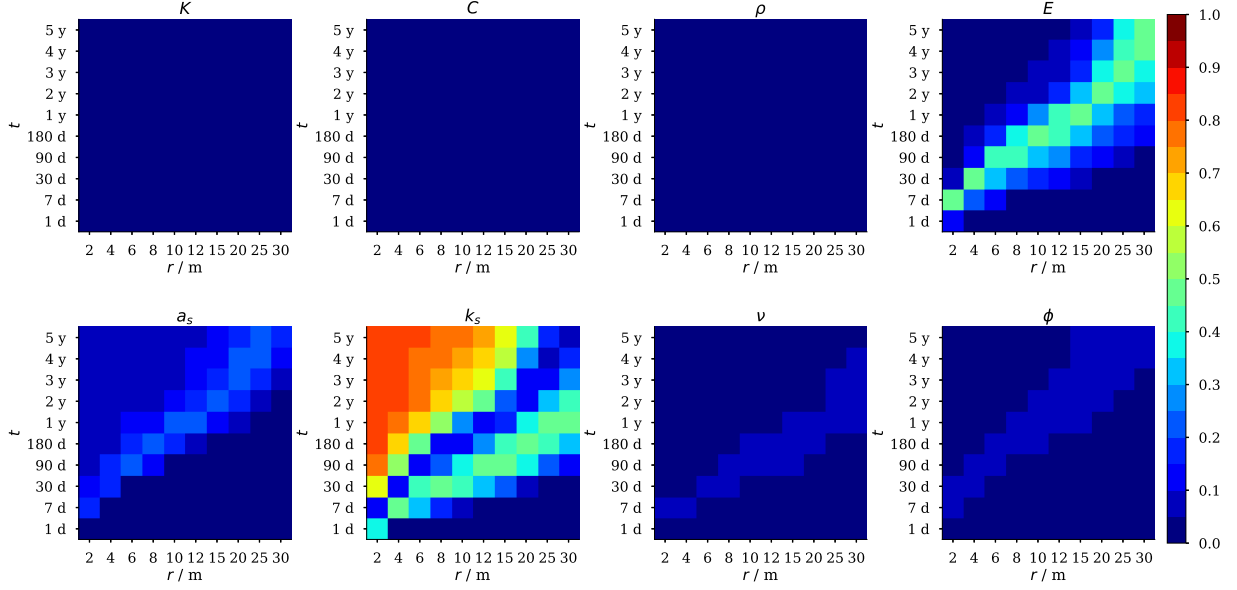
17

Figure 12: S_i for p for all combinations of r and t.

Physical interpretation of parameter sensitivity in case of pressure might not be as simple and intuitive as compared to temperature due to the various THM couplings involved. We observe by inserting Eq. 4 into Eq. 5 that the last terms on left hand side of Eqs. 1 and 5 are of same type (Laplacian of T and p, respectively). Thereby, the similarity of the sensitivity patterns for p to k_s and K to T can be explained. Furthermore, as the first term on left hand side of Eq. 1 vanishes due to the incompressibility assumption ($\beta = 0$), the sensitivity of pressure to parameters other than k_s can be attributed to the thermal and mechanical coupling terms (second and third terms on left hand side of Eq. 5, respectively). Since both of these coupling terms are transient in nature, the sensitivity to the corresponding parameters vanishes as soon as a quasi-steady state is reached. Due to the presence of coupling terms, the sensitivity attribution due to parameter interactions is not only stronger but also more diverse than observed for temperature. Fig. 13 thus does not only show the effect of interactions between closely related material parameters such as E and ν but also interactions due to couplings e.g. E-k_s or k_s-ν. This reflects that the hydro-mechanical coupling strength—manifesting itself in phenomena such as fluid load support or flow-dependent viscoelasticity—is a function of both the stiffness and the permeability of a porous medium. The sensitivity contribution due to these transient interactions gradually vanishes for most input parameter combinations, although the effects of interactions appear to last longer than in case of temperature, e.g. E-k_s, which may be indicative of slightly different intrinsic time scales of the thermal and hydraulic processes, although the transient development is dominated by the temperature signal.

5.5. Spatio-temporal sensitivity maps—radial displacement

Figs. 14 and 15 show the discrete surface charts for S_i and S_{ij}, respectively, in case of displacement u_r. In contrast to the case of T and p, the sensitivity chart for u_r shows a completely different pattern, especially in the earlier stages of time in far field. A reason for this behaviour may be that the solid skeleton reacts faster to a change in the displacement caused near the heat source. To further understand this, it is helpful to consider the analytical solution for various combinations of r and t as shown in Fig. 2. At $r = 30$ m, i.e. the point farthest from the heat source, there is a consistent increase in displacement for all times which is not the case with T and p. This also explains the sensitivity of u_r to a_s, C and ϕ (right most column for a_s, C and ϕ in Fig. 14) which will remain significant as long as there is any change in u_r with time. Likewise, the sensitivity of u_r to a_s, C and ϕ at $r = 2$ m vanishes very early (left most column for a_s, C and ϕ in
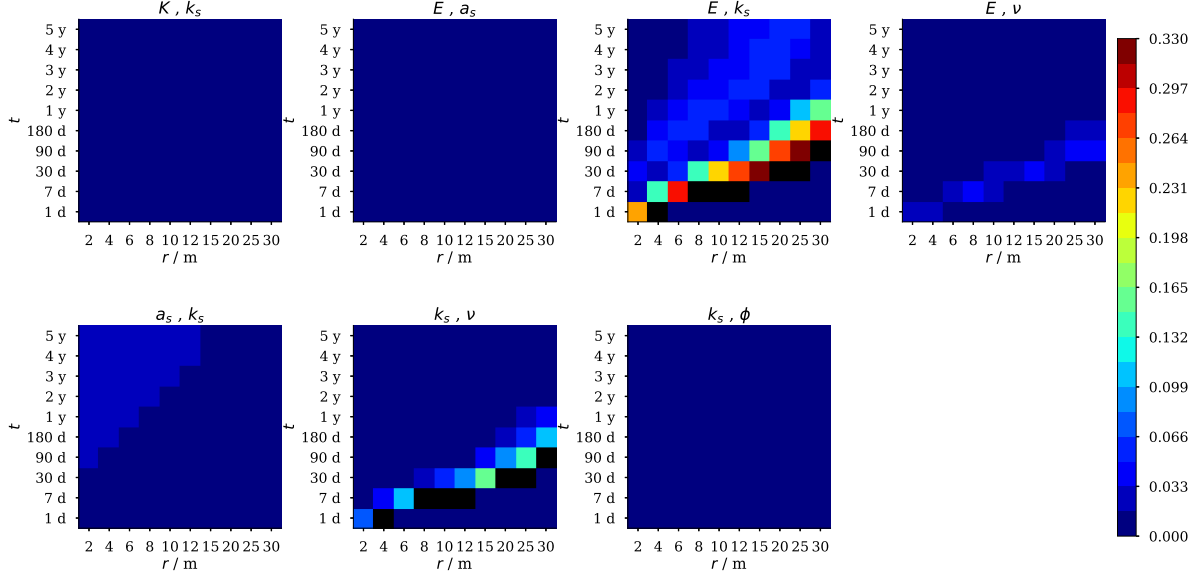
Figure 13: S_{ij} for p for all combinations of r and t.

Fig. 14) because the value of u_r in the proximity of the heater stabilises soon (Fig. 2). All three parameters are related to TM coupling: C determines the temperature evolution, $a_{\rm s}$ controls the thermal expansion of the solid skeleton. The porosity, in turn, controls the overall thermal expansion coefficient by a mixture rule and thus also affects the thermal pressurization of the fluid, which in turn affects displacements and is thus a full THM coupling effect.

The sensitivity of u_r to $k_{\rm s}$ appears to arise from the HM-coupling and thus follows a somewhat similar pattern to $k_{\rm s}$-p but with a clear dominance in the transient period. One important aspect which might have been easily overlooked by OVAT analysis is that at later times, the input parameter which mainly contributes to the sensitivity of u_r is K which is indicative of TM coupling which becoming dominant in comparison to HM-coupling in the wake of the heat front where u_r becomes sensitive to K just as temperature becomes sensitive mostly to K (Fig. 10). Fig. 15 shows interactions between E-$k_{\rm s}$ and $a_{\rm s}$-$k_{\rm s}$ in case of u_r but the scale of these interactions is very small (maximum value of $S_{ij} = 0.015$).

5.6. Overall ranking

Finally, it may be useful to have an overall view of the ranking of parameter sensitivity for all output parameters (observation quantities) based on the GSA results. Fig. 16 shows the maximum values of S_i for each input parameter among all combinations of r and t ranked from left to right. In other words, the obtained maximum values will usually occur at different locations and times. For temperature we confirm the already discussed results: the two thermal parameters control temperature. For pressure, we also find the usual intuition confirmed by identifying permeability, Young's modulus and solid thermal expansivity as the dominant parameters. Note that this corresponds to a process intrinsic parameter being the most important, following a HM-coupling and a TH(M)-coupling parameter. For displacement we observe that all leading sensitivities are related to various kinds of THM coupling. This is likely rooted in the fact that this problem is free of external load changes and instead primarily heat-source driven.

6. Concluding remarks

In this work, we performed spatio-temporal local (OVAT) and global sensitivity analyses (GSA) of a coupled THM problem. For this purpose, we employed an analytical solution [45, 46] describing the non-
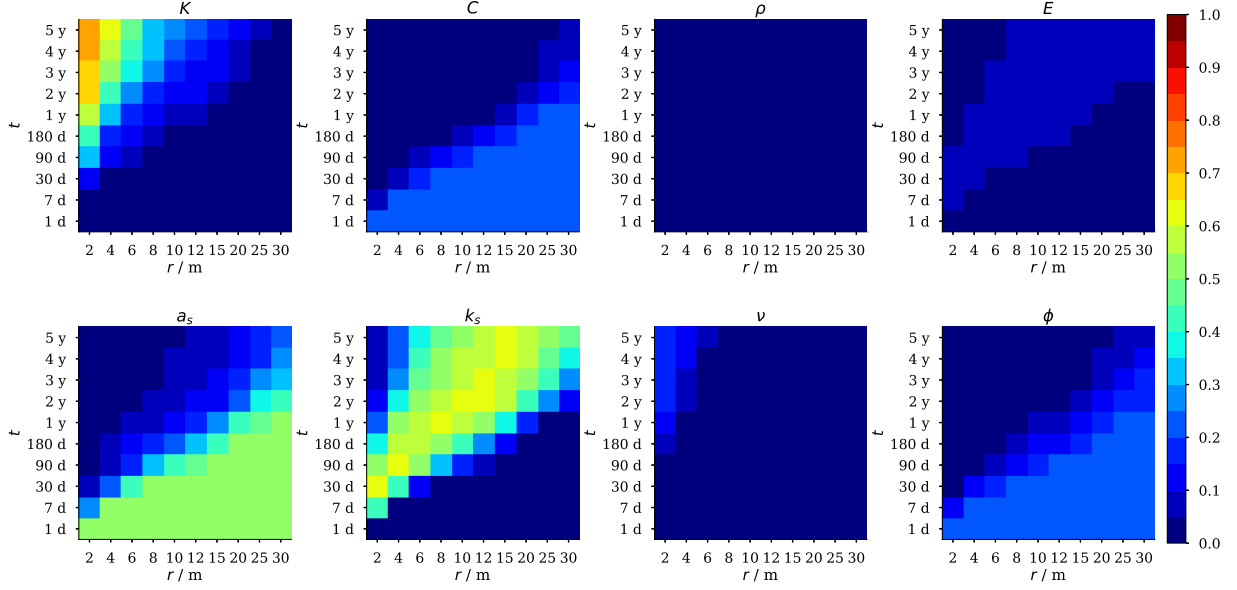
Figure 14: S_i for u_r for all combinations of r and t.

isothermal consolidation around a point heat source embedded in a fully-saturated isotropic porous medium which, in the context of nuclear waste disposal, mimics a disposal cell emitting decay heat embedded in a fluid-saturated rock type such as clay rock. As input parameters, various types of distributions obtained from the in-situ experiments were utilized [36, 48].

We showed that the OVAT screening based on the Tornado charts may underestimate the parameter sensitivity for non-monotonic parameters but can provide a sound first impression at low cost in simple cases. However, for a spatio-temporal analysis, the interpretation of results may not be easy and may require the introduction of derived sensitivity measures. Generally, the screening based on the Tornado charts should only be interpreted as a sensitivity measure very carefully. OVAT analysis can help identifying the directionality of a parameter's influence, especially when the interval is subdivided into several evaluation points. In that case, physical bounds of system response variables can be better assessed. However, real bounds may still be missed because parameter interaction is not accounted for. OVAT can severely underestimate
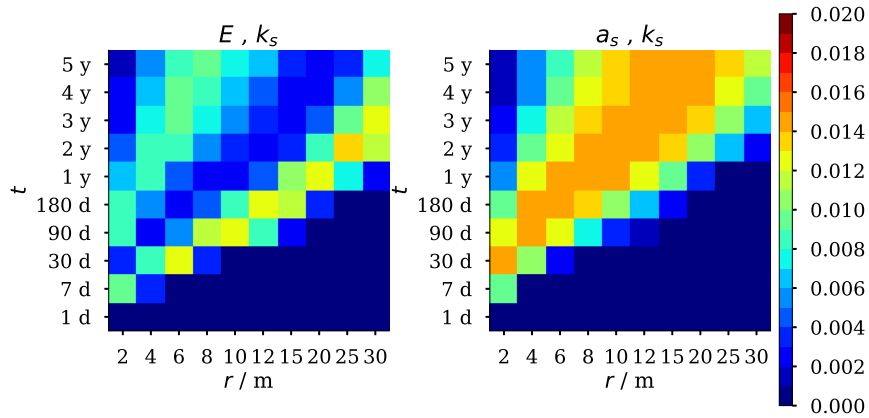

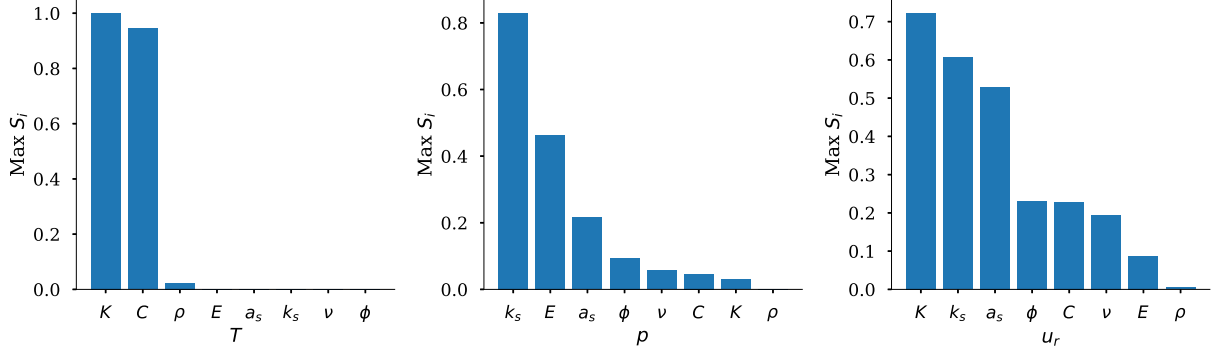Figure 15: S_{ij} for u_r for all combinations of r and t.

20

Figure 16: Maximum sensitivity (S_i) of each input parameter for all combinations of r and t

the parameter sensitivity for non-monotonic parameters as well as due to the curse of dimensionality by not including the effect of parameter interactions.

For global sensitivity analysis, we employed variance-based GSA technique which computes the so-called Sobol sensitivity indices. The main advantages of GSA are the quantitative nature of the method, the inclusion of parameter interactions and consideration of overall parameter space while the disadvantages are related to the lack of information about directionality and its change as well as high computational time. For the effective interpretation of the results, we showed that traditional bar charts may not be suitable for problems evolving in space and time. Instead, spatio-temporal sensitivity maps proved to be a valuable interpretative tool. The applicability of these charts extends to parameter interaction sensitivity. By examining the first- and second-order sensitivities as well as the ranking of sensitivity indices based on their overall maximum values it became clear that certain processes are indeed dominated by process coupling. While this is straight forward to understand in the present case, it may be less obvious in more complex scenarios where the tools developed here can significantly aid the interpretation of complex simulation results.

Based on the above findings, it can be concluded in general that neither the local sensitivity analysis, nor the global sensitivity analysis present a full picture of the parameter sensitivity of the underlying problem and thus, both should be combined to be performed side by side for an effective decision making.

We close by remarking that the spatio-temporal sensitivity maps illustrated in this study provide a valuable tool to devise monitoring strategies, as they are indicative of where sensors should be placed and when their signals should be primarily evaluated in order to obtain measurements most suitable for the determination of certain material properties or the measurement of specified target quantities. We also observed that a detailed spatio-temporal SA recovers the physical characteristics of the problem. This implies that such an analysis can help build understanding and perform causality or plausibility tests of black-box models *not* based on known PDEs, such as data-driven approaches based on, e.g., machine learning [60, 61].

Appendix A. Origin of Sobol's indices

A system under analysis involves three basic constituents; uncertain input parameters or factors, the main model under study which can be numerical or analytical, and the model output. Mathematically, this can be represented as $Y = f(X)$ where $X = (X_i, ..., X_n)$ represents the space of n input parameters (Tab. 1

in our case), f represents the model under study (THM analytical solution in our case), and Y represents the model output (T, p and u_r in our case). As the name indicates, the variance-based GSA is built around the decomposition of the total variance of the model output, which following [55, 62], can be written as

$$V(Y) = \sum_i V_i(Y) + \sum_i \sum_{j>i} V_{ij}(Y) + ... + V_{12...n}(Y) \tag{A.1}$$

where V refers to the unconditional or total variance while the terms on right hand side are referred to as partial variances related to the corresponding input factors (in subscripts) and their interactions (indicated by multiple subscripts). Thus, the definition of the sensitivity indices follows from the above equation by dividing the variance decomposition by the total variance on both sides[62] yielding the sensitivity index definition

$$S_{ij...n} = \frac{V_{ij...n}(Y)}{V(Y)} \tag{A.2}$$

In the current work, we restrict ourselves to first and second-order sensitivity indices which are simply written as

$$S_i = \frac{V_i(Y)}{V(Y)} \quad , \quad S_{ij|_{i\neq j}} = \frac{V_{ij}(Y)}{V(Y)} \tag{A.3}$$

Following [55, 62, 59], the variances in the above equation can also be expressed

$$V_i(Y) = V_{X_i}(E_{\mathbf{X}_{\sim i}}(Y \mid X_i)) \tag{A.4}$$

$$V_{ij}(Y) = V_{X_{i,j}}(E_{\mathbf{X}_{\sim i,j}}(Y \mid X_i, X_j)) - V_i(Y) - V_j(Y) \tag{A.5}$$

where $\mathbf{X}_{\sim i}$ represents the vector of all parameters excluding X_i while V and E stand for variance and expectation value, respectively. In Eq. (A.4), the expectation value E (inner term) is calculated by fixing X_i in the model input and then taking the mean of response variable Y by varying all input parameters other than X_i. This is repeated for all X_i and the variance V_{X_i} (outer term) is then computed for all these calculations. It becomes clear how the entire parameter space can be covered by this approach. Eq. (A.5) can be understood analogously. The sensitivity indices can then be rewritten as

$$S_i = \frac{V_{X_i}(E_{\mathbf{X}_{\sim i}}(Y|X_i))}{V(Y)} \tag{A.6}$$

$$S_{ij|_{i\neq j}} = \frac{V_{X_{i,j}}(E_{\mathbf{X}_{\sim i,j}}(Y \mid X_i, X_j))}{V(Y)} - S_i - S_j \tag{A.7}$$

The first-order index S_i is thus a measure of the partial variance contributed by a single parameter i to the overall variance in the response variable, while the second-order index gives a measure of the partial variance contributed by the interaction of two parameters i, j to the overall variance. In the sequel, S_{ij} will refer to $S_{ij|_{i\neq j}}$. Another important measure of the sensitivity index of an input parameter is the total effect index or total order index which is the sum of a parameter's first or main-order index and its higher-order interactions with other input parameters, i.e.

$$S_{\mathrm{T}\,i} = S_i + \sum S_{ij} + \sum S_{ij...n} \tag{A.8}$$

Following [59], it can be computed directly as

$$S_{\mathrm{T}\,i} = \frac{E_{\mathbf{X}_{\sim i}}(V_{X_i}(Y|\mathbf{X}_{\sim i}))}{V(Y)} \tag{A.9}$$

Appendix B. Computation of indices

The GSA in this work is performed using the open-source Python library SALib [63]. For sampling of the input parameter space, the code uses an improved version of the low-discrepancy quasi-random sampling scheme based on Sobol's sequence [64] by Saltelli et al. [59]. The discussion related to different sampling schemes as well as their comparison is out of the scope of this work and can be found in [65]. The formulation employed by the code uses equation (b) for S_i and equation (f) for $S_{\mathrm{T}\,i}$ in Table 2 of [59] while S_{ij} is computed following [62]. For N samples and n input parameters, the computational cost is $N(n+2)$ if only S_i is computed while $N(2n+2)$ if S_{ij} needs to be evaluated too. To check for convergence, the code also makes use of bootstrapping [66] to compute MC confidence intervals of sensitivity indices. Discussion related to why MC bootstrapping technique is preferable over MC probable error estimation can be found in [67]. Intuitively, the number of sensitivity indices obtained in case of S_i and $S_{\mathrm{T}\,i}$ each, will be equal to the number of parameters n while in case of S_{ij}, it will generate indices for $\frac{n}{2}(n-1)$ pairs (e.g. 28 for $n = 8$ in our case). Although the code provides support for simple non-uniform distributions of inputs, we rather used our own extension to also include support for truncated normal distributions. The extended code is tested for performance and correctness using the commonly employed test case of Ishigami's function [68].

References

[1] Melissa A Sanchez and Sally M Blower. Uncertainty and sensitivity analysis of the basic reproductive rate: tuberculosis as an example. *American journal of epidemiology*, 145(12):1127–1137, 1997.

[2] Xiao-jiang Feng, Sara Hooshangi, David Chen, Genyuan Li, Ron Weiss, and Herschel Rabitz. Optimizing genetic circuits by global sensitivity analysis. *Biophysical journal*, 87(4):2195–2202, 2004.

[3] Vinzenz Gregor Eck, Wouter Paulus Donders, Jacob Sturdy, Jonathan Feinberg, Tammo Delhaas, Leif Rune Hellevik, and Wouter Huberts. A guide to uncertainty quantification and sensitivity analysis for cardiovascular applications. *International Journal for Numerical Methods in Biomedical Engineering*, 32(8):e02755, 2016. doi: 10.1002/cnm.2755. URL https://onlinelibrary.wiley.com/doi/abs/10.1002/cnm.2755. e02755 cnm.2755.

[4] Pietro Ceccato, Nadine Gobron, Stéphane Flasse, Bernard Pinty, and Stefano Tarantola. Designing a spectral index to estimate vegetation water content from remote sensing data: Part 1: Theoretical approach. *Remote sensing of environment*, 82(2-3):188–197, 2002.

[5] H De Moel, NEM Asselman, and JCJH Aerts. Uncertainty and sensitivity analysis of coastal flood damage estimates in the west of the netherlands. *Natural Hazards and Earth system sciences*, 12(4):1045, 2012.

[6] JD Herman, JB Kollat, PM Reed, and T Wagener. Method of morris effectively reduces the computational demands of global sensitivity analysis for distributed watershed models. *Hydrology & Earth System Sciences Discussions*, 10(4), 2013.

[7] MPR Haaker and PJT Verheijen. Local and global sensitivity analysis for a reactor design with parameter uncertainty. *Chemical Engineering Research and Design*, 82(5):591–598, 2004.

[8] Genyuan Li, Herschel Rabitz, Paul E Yelvington, Oluwayemisi O Oluwole, Fred Bacon, Charles E Kolb, and Jacqueline Schoendorf. Global sensitivity analysis for systems with independent and/or correlated inputs. *The journal of physical chemistry a*, 114(19):6022–6032, 2010.

[9] Jinkyung Kim, Matthew J. Realff, and Jay H. Lee. Optimal design and global sensitivity analysis of biomass supply chain networks for biofuels under uncertainty. *Computers & Chemical Engineering*, 35(9):1738 – 1751, 2011. ISSN 0098-1354. doi: https://doi.org/10.1016/j.compchemeng.2011.02.008. URL http://www.sciencedirect.com/science/article/pii/S0098135411000706. Energy Systems Engineering.

[10] Kendall C DeJonge, James C Ascough II, Mehdi Ahmadi, Allan A Andales, and Mazdak Arabi. Global sensitivity and uncertainty analysis of a dynamic agroecosystem model under different irrigation treatments. *Ecological Modelling*, 231: 113–125, 2012.

[11] MA Vazquez-Cruz, R Guzman-Cruz, IL Lopez-Cruz, O Cornejo-Perez, I Torres-Pacheco, and RG Guevara-Gonzalez. Global sensitivity analysis by means of efast and sobol'methods and calibration of reduced state-variable tomgro model using genetic algorithms. *Computers and Electronics in Agriculture*, 100:1–12, 2014.

[12] Gang Zhao, Brett A Bryan, and Xiaodong Song. Sensitivity and uncertainty analysis of the apsim-wheat model: Interactions between cultivar, environmental, and management parameters. *Ecological Modelling*, 279:1–11, 2014.

[13] Enrique Carrero, Nestor V Queipo, Salvador Pintos, and Luis E Zerpa. Global sensitivity analysis of alkali–surfactant–polymer enhanced oil recovery processes. *Journal of Petroleum Science and Engineering*, 58(1-2):30–42, 2007.

[14] Zhenxue Dai, Hari Viswanathan, Julianna Fessenden-Rahn, Richard Middleton, Feng Pan, Wei Jia, Si-Yong Lee, Brian McPherson, William Ampomah, and Reid Grigg. Uncertainty quantification for co2 sequestration and enhanced oil recovery. *arXiv preprint arXiv:1411.4900*, 2014.

[15] W Ampomah, RS Balch, M Cather, R Will, D Gunda, Z Dai, and MR Soltanian. Optimum design of co2 storage and oil recovery under geological uncertainty. *Applied Energy*, 195:80–92, 2017.

[16] Katelyn Kring and Snehamoy Chatterjee. Uncertainty quantification of structural and geotechnical parameter by geostatistical simulations applied to a stability analysis case study with limited exploration data. *International Journal of Rock Mechanics and Mining Sciences*, 125:104157, 2020.

[17] Nut Mao, Tamara Al-Bittar, and Abdul-Hamid Soubra. Probabilistic analysis and design of strip foundations resting on rocks obeying hoek–brown failure criterion. *International Journal of Rock Mechanics and Mining Sciences*, 49:45–58, 2012.

[18] Morteza Beiki, Ali Bashari, and Abbas Majdi. Genetic programming approach for estimating the deformation modulus of rock mass using sensitivity analysis by neural network. *International journal of rock mechanics and mining sciences*, 47(7):1091–1103, 2010.

[19] P Starzec and J Andersson. Application of two-level factorial design to sensitivity analysis of keyblock statistics from fracture geometry. *International Journal of Rock Mechanics and Mining Sciences*, 39(2):243–255, 2002.

[20] L. Jing, C.-F. Tsang, and O. Stephansson. Decovalex—an international co-operative research project on mathematical models of coupled thm processes for safety analysis of radioactive waste repositories. *International Journal of Rock Mechanics and Mining Sciences & Geomechanics Abstracts*, 32(5):389 – 398, 1995. ISSN 0148-9062. doi: https://doi.org/10.1016/0148-9062(95)00031-B. URL http://www.sciencedirect.com/science/article/pii/014890629500031B. Thermo-Hydro-Mechanical Coupling in Rock Mechanics.

[21] Chin-Fu Tsang, JD Barnichon, J Birkholzer, Xiang Ling Li, HH Liu, and X Sillen. Coupled thermo-hydro-mechanical processes in the near field of a high-level radioactive waste repository in clay formations. *International Journal of Rock Mechanics and Mining Sciences*, 49:31–44, 2012.

[22] Ove Stephansson, John Hudson, and Lanru Jing. *Coupled thermo-hydro-mechanical-chemical processes in Geo-Systems*, volume 2. Elsevier, 2004.

[23] A Uchaipichat and N Khalili. Experimental investigation of thermo-hydro-mechanical behaviour of an unsaturated silt. *Géotechnique*, 59(4):339–353, 2009.

[24] William KS Pao, Roland W Lewis, and Ian Masters. A fully coupled hydro-thermo-poro-mechanical model for black oil

reservoir simulation. *International Journal for Numerical and Analytical Methods in Geomechanics*, 25(12):1229–1256, 2001.

[25] A Lloret and MV Villar. Advances on the knowledge of the thermo-hydro-mechanical behaviour of heavily compacted "febex" bentonite. *Physics and Chemistry of the Earth, Parts A/B/C*, 32(8–14):701–715, 2007.

[26] X. Y. Miao, C. Beyer, U. J. Görke, O. Kolditz, H. Hailemariam, and T. Nagel. Thermo-hydro-mechanical analysis of cement-based sensible heat stores for domestic applications. *Environmental Earth Sciences*, 75(18):1293, 2016.

[27] O. Kolditz, U.-J. Görke, H. Shao, and W. Wang. *Thermo-hydro-mechanical-chemical processes in porous media: benchmarks and examples*, volume 86. Springer Science & Business Media, 2012.

[28] Ruiping Guo, KE Thatcher, DM Seyedi, and C Plúa. Calibration of the thermo-hydro-mechanical parameters of the callovo-oxfordian claystone and the modelling of the alc experiment. *International Journal of Rock Mechanics and Mining Sciences*, 132:104351, 2020.

[29] Jung-Wook Park, Jonny Rutqvist, Dongwoo Ryu, Eui-Seob Park, and Joong-Ho Synn. Coupled thermal-hydrological-mechanical behavior of rock mass surrounding a high-temperature thermal energy storage cavern at shallow depth. *International Journal of Rock Mechanics and Mining Sciences*, 83:149–161, 2016.

[30] Jung-Wook Park, Yves Guglielmi, Bastian Graupner, Jonny Rutqvist, Taehyun Kim, Eui-Seob Park, and Changsoo Lee. Modeling of fluid injection-induced fault reactivation using coupled fluid flow and mechanical interface model. *International Journal of Rock Mechanics and Mining Sciences*, 132:104373, 2020.

[31] Ola Karnland, Torbjörn Sandén, Lars-Erik Johannesson, Trygve E Eriksen, Mats Jansson, Susanna Wold, Karsten Pedersen, Mehrdad Motamedi, and Bo Rosborg. Long term test of buffer material. final report on the pilot parcels. Technical report, Swedish Nuclear Fuel and Waste Management Co., 2000.

[32] X.L. Li, W. Bastiaens, P. Van Marcke, J. Verstricht, G.J. Chen, E. Weetjens, and X. Sillen. Design and development of large-scale in-situ praclay heater test and horizontal high-level radioactive waste disposal gallery seal test in belgian hades. *Journal of Rock Mechanics and Geotechnical Engineering*, 2(2):103 – 110, 2010. ISSN 1674-7755. doi: https://doi.org/10.3724/SP.J.1235.2010.00103. URL http://www.sciencedirect.com/science/article/pii/S1674775515300317.

[33] J. Pacovský, J. Svoboda, and L. Zapletal. Saturation development in the bentonite barrier of the mock-up-cz geotechnical experiment. *Physics and Chemistry of the Earth, Parts A/B/C*, 32(8):767 – 779, 2007. ISSN 1474-7065. doi: https://doi.org/10.1016/j.pce.2006.03.005. URL http://www.sciencedirect.com/science/article/pii/S1474706506002038. Clay in natural and engineered barriers for radioactive waste confinement - Part 2.

[34] Yuemiao Liu, Like Ma, Dan Ke, Shengfei Cao, Jingli Xie, Xingguang Zhao, Liang Chen, and Panpan Zhang. Design and validation of the thmc china-mock-up test on buffer material for hlw disposal. *Journal of Rock Mechanics and Geotechnical Engineering*, 6(2):119 – 125, 2014. ISSN 1674-7755. doi: https://doi.org/10.1016/j.jrmge.2014.01.004. URL http://www.sciencedirect.com/science/article/pii/S1674775514000134.

[35] Paul Bossart, David Jaeggi, and Christophe Nussbaum. Experiments on thermo-hydro-mechanical behaviour of Opalinus Clay at Mont Terri rock laboratory, Switzerland. *Journal of Rock Mechanics and Geotechnical Engineering*, 9(3):502–510, jun 2017. ISSN 16747755. doi: 10.1016/j.jrmge.2016.11.014.

[36] G. Armand, F. Bumbieler, N. Conil, R. de la Vaissiére, J.-M. Bosgiraud, and M.-N. Vu. Main outcomes from in situ thermo-hydro-mechanical experiments programme to demonstrate feasibility of radioactive high-level waste disposal in the callovo-oxfordian claystone. *Journal of Rock Mechanics and Geotechnical Engineering*, 9(3):415–427, 2017.

[37] Ju Wang, Liang Chen, Rui Su, and Xingguang Zhao. The Beishan underground research laboratory for geological disposal of high-level radioactive waste in China: Planning, site selection, site characterization and in situ tests. *Journal of Rock Mechanics and Geotechnical Engineering*, 10(3):411–435, jun 2018. ISSN 16747755. doi: 10.1016/j.jrmge.2018.03.002.

[38] J.C. Helton, J.D. Johnson, C.J. Sallaberry, and C.B. Storlie. Survey of sampling-based methods for uncertainty and sensitivity analysis. *Reliability Engineering & System Safety*, 91(10):1175 – 1209, 2006. ISSN 0951-8320. doi: https://doi.org/10.1016/j.ress.2005.11.017. URL http://www.sciencedirect.com/science/article/pii/S0951832005002292. The Fourth International Conference on Sensitivity Analysis of Model Output (SAMO 2004).

[39] Norihiro Watanabe, Wenqing Wang, Christopher I McDermott, Takeo Taniguchi, and Olaf Kolditz. Uncertainty analysis of thermo-hydro-mechanical coupled processes in heterogeneous porous media. *Computational Mechanics*, 45(4):263, 2010.

[40] Long Nguyen-Tuan, Tom Lahmer, Maria Datcheva, Eugenia Stoimenova, and Tom Schanz. A novel parameter identification approach for buffer elements involving complex coupled thermo-hydro-mechanical analyses. *Computers and Geotechnics*, 76:23 – 32, 2016. ISSN 0266-352X. doi: https://doi.org/10.1016/j.compgeo.2016.02.005. URL http://www.sciencedirect.com/science/article/pii/S0266352X16300143.

[41] Fabrice Dupray, Chao Li, and Lyesse Laloui. Thm coupling sensitivity analysis in geological nuclear waste storage. *Engineering geology*, 163:113–121, 2013.

[42] K. Khaledi, E. Mahmoudi, M. Datcheva, D. König, and T. Schanz. Sensitivity analysis and parameter identification of a time dependent constitutive model for rock salt. *Journal of Computational and Applied Mathematics*, 293:128 – 138, 2016. ISSN 0377-0427. doi: https://doi.org/10.1016/j.cam.2015.03.049. URL http://www.sciencedirect.com/science/article/pii/S0377042715002022. Efficient Numerical Methods for Large-scale Scientific Computations.

[43] SN Pandey and Vikram Vishal. Sensitivity analysis of coupled processes and parameters on the performance of enhanced geothermal systems. *Scientific reports*, 7(1):1–14, 2017.

[44] Long Nguyen-Tuan, Tom Lahmer, Maria Datcheva, and Tom Schanz. Global and local sensitivity analyses for coupled thermo–hydro–mechanical problems. *International Journal for Numerical and Analytical Methods in Geomechanics*, 41 (5):707–720, 2017.

[45] J. R. Booker and C. Savvidou. Consolidation around a point heat source. *International Journal for Numerical and Analytical Methods in Geomechanics*, 9(2):173–184, 1985.

[46] A. A. Chaudhry, J. Buchwald, O. Kolditz, and T. Nagel. Consolidation around a point heat source (correction and

verification). *International Journal for Numerical and Analytical Methods in Geomechanics*, pages 1–9, 2019. doi: 10.1002/nag.2998. URL https://doi.org/10.1002/nag.2998.

[47] Roland Wynne Lewis and Bernard A Schrefler. *The finite element method in the static and dynamic deformation and consolidation of porous media*. John Wiley, 1998.

[48] C. Plúa, V. Manon, D. Seyedi, G. Armand, J. Rutqvist, J. Birkholzer, H. Xu, R. Guo, K.E. Tatcher, A.E. Bond, W. Wang, T. Nagel, H. Shao, and O. Kolditz. Decovalex-2019 task e final report. Technical report, DECOVALEX, 2020. LBNL-2001265.

[49] Andrea Saltelli, Ksenia Aleksankina, William Becker, Pamela Fennell, Federico Ferretti, Niels Holst, Sushan Li, and Qiongli Wu. Why so many published sensitivity analyses are false: A systematic review of sensitivity analysis practices. *Environmental modelling & software*, 114:29–39, 2019.

[50] Max D. Morris. Factorial sampling plans for preliminary computational experiments. *Technometrics*, 33(2):161–174, 1991. doi: 10.1080/00401706.1991.10484804.

[51] Francesca Campolongo, Jessica Cariboni, and Andrea Saltelli. An effective screening design for sensitivity analysis of large models. *Environmental Modelling & Software*, 22(10):1509 – 1518, 2007. ISSN 1364-8152. doi: https://doi.org/10.1016/j.envsoft.2006.10.004. URL http://www.sciencedirect.com/science/article/pii/S1364815206002805. Modelling, computer-assisted simulations, and mapping of dangerous phenomena for hazard assessment.

[52] Emanuele Borgonovo. A new uncertainty importance measure. *Reliability Engineering & System Safety*, 92(6):771–784, 2007.

[53] I.M. Sobol' and S. Kucherenko. Derivative based global sensitivity measures and their link with global sensitivity indices. *Mathematics and Computers in Simulation*, 79(10):3009 – 3017, 2009. ISSN 0378-4754. doi: https://doi.org/10.1016/j.matcom.2009.01.023. URL http://www.sciencedirect.com/science/article/pii/S0378475409000354.

[54] R. I. Cukier, C. M. Fortuin, K. E. Shuler, A. G. Petschek, and J. H. Schaibly. Study of the sensitivity of coupled reaction systems to uncertainties in rate coefficients. i theory. *The Journal of Chemical Physics*, 59(8):3873–3878, 1973. doi: 10.1063/1.1680571. URL https://doi.org/10.1063/1.1680571.

[55] I.M Sobol. Global sensitivity indices for nonlinear mathematical models and their monte carlo estimates. *Mathematics and Computers in Simulation*, 55(1):271 – 280, 2001. ISSN 0378-4754. doi: https://doi.org/10.1016/S0378-4754(00)00270-6. URL http://www.sciencedirect.com/science/article/pii/S0378475400002706. The Second IMACS Seminar on Monte Carlo Methods.

[56] Andrea Saltelli and Ricardo Bolado. An alternative way to compute fourier amplitude sensitivity test (fast). *Computational Statistics & Data Analysis*, 26(4):445 – 460, 1998. ISSN 0167-9473. doi: https://doi.org/10.1016/S0167-9473(97)00043-1. URL http://www.sciencedirect.com/science/article/pii/S0167947397000431.

[57] Andrea Saltelli, Stefano Tarantola, Francesca Campolongo, and Marco Ratto. *Sensitivity analysis in practice: a guide to assessing scientific models*, volume 1. Wiley Online Library, 2004.

[58] Graham Glen and Kristin Isaacs. Estimating sobol sensitivity indices using correlations. *Environmental Modelling & Software*, 37:157–166, 2012.

[59] Andrea Saltelli, Paola Annoni, Ivano Azzini, Francesca Campolongo, Marco Ratto, and Stefano Tarantola. Variance based sensitivity analysis of model output. design and estimator for the total sensitivity index. *Computer Physics Communications*, 181(2):259–270, feb 2010. ISSN 00104655. doi: 10.1016/j.cpc.2009.09.018.

[60] T. Kirchdoerfer and M. Ortiz. Data-driven computational mechanics. *Computer Methods in Applied Mechanics and Engineering*, 304:81–101, jun 2016. ISSN 00457825. doi: 10.1016/j.cma.2016.02.001. URL https://linkinghub.elsevier.com/retrieve/pii/S0045782516300238.

[61] Wentao Yan, Stephen Lin, Orion L. Kafka, Yanping Lian, Cheng Yu, Zeliang Liu, Jinhui Yan, Sarah Wolff, Hao Wu, Ebot Ndip-Agbor, Mojtaba Mozaffar, Kornel Ehmann, Jian Cao, Gregory J. Wagner, and Wing Kam Liu. Data-driven multi-scale multi-physics models to derive process–structure–property relationships for additive manufacturing. *Computational Mechanics*, 61(5):521–541, may 2018. ISSN 0178-7675. doi: 10.1007/s00466-018-1539-z. URL https://doi.org/10.1007/s00466-018-1539-zhttp://link.springer.com/10.1007/s00466-018-1539-z.

[62] Andrea Saltelli. Making best use of model evaluations to compute sensitivity indices. *Computer Physics Communications*, 145(2):280 – 297, 2002. ISSN 0010-4655. doi: https://doi.org/10.1016/S0010-4655(02)00280-1. URL http://www.sciencedirect.com/science/article/pii/S0010465502002801.

[63] Jon Herman and Will Usher. Salib: An open-source python library for sensitivity analysis. *Journal of Open Source Software*, 2(9):97, 2017. doi: 10.21105/joss.00097. URL https://doi.org/10.21105/joss.00097.

[64] I.M Sobol'. On the distribution of points in a cube and the approximate evaluation of integrals. *USSR Computational Mathematics and Mathematical Physics*, 7(4):86 – 112, 1967. ISSN 0041-5553. doi: https://doi.org/10.1016/0041-5553(67)90144-9. URL http://www.sciencedirect.com/science/article/pii/0041555367901449.

[65] Andrea Saltelli, Marco Ratto, Terry Andres, Francesca Campolongo, Jessica Cariboni, Debora Gatelli, Michaela Saisana, and Stefano Tarantola. *Global sensitivity analysis: the primer*. John Wiley & Sons, 2008.

[66] Anthony Christopher Davison and David Victor Hinkley. *Bootstrap methods and their application*, volume 1. Cambridge university press, 1997.

[67] G. E. B. Archer, A. Saltelli, and I. M. Sobol. Sensitivity measures, anova-like techniques and the use of bootstrap. *Journal of Statistical Computation and Simulation*, 58(2):99–120, 1997. doi: 10.1080/00949659708811825.

[68] T. Ishigami and T. Homma. An importance quantification technique in uncertainty analysis for computer models. In *Proceedings. First International Symposium on Uncertainty Modeling and Analysis*, pages 398–403, 1990.